

Air Force Institute of Technology

AFIT Scholar

Theses and Dissertations


Student Graduate Works

3-9-2009

Advanced Radiometry for High Discrimination Explosive Fireball Discrimination

Steven E. Slagle

Follow this and additional works at: <https://scholar.afit.edu/etd>

 Part of the [Electromagnetics and Photonics Commons](#), [Materials Chemistry Commons](#), and the [Radiochemistry Commons](#)

Recommended Citation

Slagle, Steven E., "Advanced Radiometry for High Discrimination Explosive Fireball Discrimination" (2009). *Theses and Dissertations*. 2447. <https://scholar.afit.edu/etd/2447>

This Thesis is brought to you for free and open access by the Student Graduate Works at AFIT Scholar. It has been accepted for inclusion in Theses and Dissertations by an authorized administrator of AFIT Scholar. For more information, please contact richard.mansfield@afit.edu.



**ADVANCED RADIOMETRY FOR HIGH EXPLOSIVE FIREBALL
DISCRIMINATION**

THESIS

Steven E. Slagle, Captain, USAF

AFIT/GEO/ENP/09-M02

**DEPARTMENT OF THE AIR FORCE
AIR UNIVERSITY**

AIR FORCE INSTITUTE OF TECHNOLOGY

Wright-Patterson Air Force Base, Ohio

APPROVED FOR PUBLIC RELEASE; DISTRIBUTION UNLIMITED

The views expressed in this thesis are those of the author and do not reflect the official policy or position of the United States Air Force, Department of Defense, or the United States Government.

AFIT/GEO/ENP/09-M02

ADVANCED RADIOMETRY FOR HIGH EXPLOSIVE FIREBALL
DISCRIMINATION

THESIS

Presented to the Faculty

Department of Engineering Physics

Graduate School of Engineering and Management

Air Force Institute of Technology

Air University

Air Education and Training Command

In Partial Fulfillment of the Requirements for the
Degree of Master of Science in Electrical Engineering

Steven E. Slagle, BS

Captain, USAF

March 2009

APPROVED FOR PUBLIC RELEASE; DISTRIBUTION UNLIMITED

ADVANCE RADIOMETRY FOR HIGH EXPLOSIVE FIREBALL
DISCRIMINATION

Steven E. Slagle, BS
Captain, USAF

Approved:



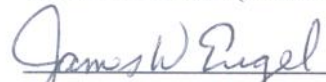
Kevin C. Gross (Chairman)

26-Mar-09
Date



Glen P. Perram (Member)

26 Mar 09
Date



James Engel (Member)

25 Mar 2009
Date

Abstract

Recently AFIT developed a high explosive (HE) fireball emission phenomenological model in the mid-wave infrared (MWIR) spectrum to perform discrimination. This consists of five physical fit parameters that describe the fireball's temperature, size, soot concentration and the selective emissions from the H₂O and CO₂ concentrations. The spectral model provided a highly correlated fit, with a relative error of 1.7% in the median, to the observed Brilliant Flash II (BFII) data that collected spectral signatures from several different TNT and enhanced novel explosives (ENEs) using a Fourier-transform spectrometer (FTS).

The following work replaces the spectral data with a combination of five-band pass filters integrated over the spectral BFII data to simulate intensities collected from a radiometer to derive the five fit parameters. Two bands were centered at 2580cm⁻¹ and 4535cm⁻¹ to employ two-color pyrometry, which calculated the color temperature. The third band was centered at 2200cm⁻¹, where the emissivity was assumed equal to one, which allowed for a separation between emissivity and area. Bands were placed at 4130cm⁻¹ and 3425cm⁻¹ in known H₂O and CO₂ emission regions to calculate their respective concentrations. Sequentially calculating each fit parameter from these five bands successfully derived temperature, size and soot concentration within 16% at t=0.6s, with the H₂O and CO₂ concentrations varying by 256% at t=0.6s. To reduce the deviation in the fit parameters two test cases were examined which moved the band widths and center positions were adjusted to 3400 cm⁻¹, 4100cm⁻¹, 4430 cm⁻¹, 5250 cm⁻¹, 6100 cm⁻¹. Calculating the color temperature first, the remaining four fit parameters were concurrently calculated, providing an estimation of the first three fit parameters to within 9.9% at t=0.6s and the H₂O and CO₂ concentrations to 17% at t=0.6s. For the two test cases examined the radiometric model produced a maximum residual of 59 W/Sr/cm⁻¹ where the spectral model produced 41 W/Sr/cm⁻¹, with the computed Hydrogen to Carbon ratio having a maximum deviation of 20% from the spectral results. This demonstrated that a combination of radiometric intensities can be used in place of the spectral data and still derive similar results. The radiometric intensities used to derive the physical fit parameters

yielded a Fisher Ratio (FR) of 23, where the raw uninterrupted intensities only yielded a FR of 4 indicating the increased benefit of interpreting the intensities into physical fit parameters.

When fewer than five radiometric bands are employed, solving for the five fit parameters becomes an unbalanced equation with respect to the current spectral model making it a non-ideal method to measure classification. A systematic search was performed to investigate classification potential using two, three and four radiometric bands combinations. The Fisher Ration (FR) was used to measure the discrimination potential between TNT and ENE fireballs. The two-band search yielded a maximum FR of 6, which provides poor classification capability between TNT and ENE. The three and four-band search highlighted a highly confined spectral region centered at 5000cm^{-1} where each band resided and partially overlapped. This region produced a FR of 41 for the three band solutions respectively, which was double all other FR calculated from band combinations outside of this region. A comparison to the spectral model was perform which shows that the current spectral model does not provide the high discrimination observed from the data in this region.

Acknowledgments

First and foremost I would like to thank my family for their endless patience and understand during this process. To Kevin Gross, my advisor, I owe a tremendous debt to for his guidance, perspective and uncanny dedication. Without his assistance the following work would not of been possible, and even it is was, it certainly wouldn't have been half as interesting or fun. I also feel obligated to thank his wife and family forgiving him for all the nights I kept him from coming home at a regular hour because he was helping me to graduate. To my committee members, Glen Perram and Jim Engle, I would like to thank them for sharing a real enthusiasm for the subject material and providing me the big picture when I had my blinders on. To the many professors at AFIT who not only contributed to my education, but growth as a person. My friends, who I have seemly ignored, alienated and almost completely disappeared from their daily lives. Your friendship has never been far from my thoughts even though I rarely answer the phone anymore. Still you have always stepped in to save me when I needed it most and I will be eternally in your debt. Lastly, but certainly not least, my dog Kaley who still hasn't left my side through all the sleepless nights, and weeks without a walk in the woods.

Steven E. Slagle

Table of Contents

	Page
Abstract	iv
Acknowledgments	vi
Table of Contents	vii
List of Figures	viii
List of Tables	xii
I. Introduction	1
1.1 Document Preview	4
II. Background	5
2.1 Experimental Data	5
2.2 Dills' Research Overview	10
III. Methodology	21
3.1 Data Matching	21
3.2 Five Radiometric Bands	22
3.3 Five band Summery	26
3.4 Multi-band Search	26
IV. Results	28
4.1 Five-Band Radiometric Results	28
4.2 Revised Radiometric Model	37
4.3 Radiometric Band Search Results	45
V. Conclusions	59
5.1 Summery of Key Finding	59
5.2 Discussion of the Key Findings	60
5.3 Future Research	62
Appendix: Interferogram Time Corrections	64
Bibliography	67

List of Figures

Figure	Page
1. Viewing geometry of the sensor suite with respect to the detonation site during BFII [1].....	6
2. Two interferogram overlaid showing the statics source, on top, in green and the evolving source below in blue with scene change artifacts present in the signal [1]	8
3. Data cube of apparent intensity from a typical munitions detonation with a degraded spectral resolution of 16cm^{-1} , reduced from 4cm^{-1} , and a temporal resolution of 8 Hz respectively [1].....	10
4. Comparison of absolute intensities collected by the MR-154, MR-354 and the radiometer for a detonation of a 100 kg ENE. The inserted plot shows the transmittance T of the used bandpass filter (black) used by the radiometer and the spectral ranged that was integrated over the transmittance of the atmosphere (grey) in that region for reference [1].	11
5. Three classes, A, B and C projected onto a Fisher Line calculated from feature F_1 and F_2 . A probability distribution functions is shown projected over the respective data points from each class from the Fisher Line. Each class variance is displayed by a solid line and the distance between the mean of each class is also indicated by a dashed line. [12].....	12
6. (a) Two classes of data described by two features with a $FR=4$; (b) Both classes of data projected on to the fisher line from FLD with their respective PDF and a $FR=4$	13
7. (a) Two classes of data described by two features with a $FR=43$; (b) Both classes of data projected on to the fisher line from FLD with their respective PDF and a $FR=43$	13
8. Simplified radiometric transmission showing typical sources of noise and losses.....	15
9. Top to bottom Panel: A comparative Planckian blackbody signature, the source and modeled intensity/The emissivity of the atmosphere/emissive spectral regions of H_2O present in the atmosphere/emissive spectral regions of CO_2 in the atmosphere/emissive spectral regions of CO in the atmosphere/ emissive spectral regions of HCl in the atmosphere/Transmittance of the atmosphere as a function of wavenumber. [1]	17
10. Temperature versus time curves obtained by fits to fireball spectra of 10 (o),50(square), 100(Δ), 1000(\diamond) kg charged of TNT. Error bars represent fit parameter uncertainties at the 95% confidence level [1].	19
11. TNT (solid black) and ENE (dashed black) probability densities based on spectrally extracted R values and assuming a normal distribution. This distribution has a calculated fisher ratio of 17.5. [1].....	19
12. All of the data sets from BFII with the 10kg events in red, 50kg in blue, 100kg in green and the 1000kg in black. Events had fewer than 5 data points and were later removed.....	22

Figure	Page
13. Show the 50kg events in blue, the 100kg events in green and the 1000kg events in black. The grey region shows the area of maximum overlap in the data where several of the 50kg events do not span and were removed from the data set for analysis.....	23
14. Top Panel: The H ₂ O, CO ₂ , soot and total emissivity is shown spectrally. The gray regions indicate the band placement for the radiometric model. Bottom Panel: The spectral transmittance of the atmosphere with the grey regions indicating band placement for the radiometric model	24
15. Panel 1 depicts a 50 kg TNT detonation from the BFII tests compared again the data collected by the MR-154 FTS spectrometer. The residuals from the model and actual data from both the radiometric and spectral model are provided in panel 2 and 3.....	29
16. Panel 1 depicts a 50 kg ENE detonation from the BFII tests compared again the data collected by the MR-154 FTS spectrometer. The residuals from the model and actual data from both the radiometric and spectral model are provided in panel 2 and 3.....	30
17. Feature comparison between radiometric and spectral model for event 164DAT40, 50kg TNT for (a) Temperature, (b) Area, (c) Soot Constant, (d) H ₂ O concentration, CO ₂ concentration	32
18. Feature comparison between radiometric and spectral model for event 164DAT43, 50kg ENE2 for (a) Temperature, (b) Area, (c) Soot Constant, (d) H ₂ O concentration, (e) HCR, and (f) CO ₂ concentration.....	33
19. The HCR for all the ENE and TNT events showing the relative separation between the two classes.....	35
20. Data projected on the fisher line with a Gaussian representation of the data projection.	36
21. Top to bottom panel: Spectral model fit to the FBII data followed by the residuals present from comparing the spectral model to the BFII data.....	38
22. Top to bottom panel: Radiometric model fit to the FBII data with the band selected shown in color followed by the residuals present from comparing the spectral model to the BFII data.	39
23. Top to bottom panel: Spectral model fit to the FBII data followed by the residuals present from comparing the spectral model to the BFII data.....	40
24. Top to bottom panel: Radiometric model fit to the FBII data with the band selected shown in color followed by the residuals present from comparing the spectral model to the BFII data.	41

Figure	Page
25. Comparison of the five fit parameters for a 50 kg TNT, event 164DAT40, depicted in blue dashed lines from the revised radiometric model compared to the spectral model shown by a solid red line for (a) temperature, (b) size, (c) soot concentration, (d) H ₂ O concentration and (e) CO ₂ concentrations	42
26. Comparison of the five fit parameters for a 50 kg ENE2, event 164DAT43, depicted in blue dashed lines from the revised radiometric model compared to the spectral model shown by a solid red line for (a) temperature, (b) size, (c) soot particulate absorption coefficient, (d) H ₂ O concentration and (e) CO ₂ concentrations.....	433
27. HCR for the revised radiometric model represented by solid red line and the spectral model represented by a solid red line for the (a) ENE and (b) TNT test cases.....	444
28. Top to bottom panel: Spectral emissivity of the fire ball in black and the soot emission in gray; spectral emissivity of H ₂ O; the spectral emissivity of CO ₂ ; spectral emissivity of CO; spectral emissivity HCl; spectral transmission of the atmosphere; grey regions representing the two best bands from the two-band search that produced a FR of 6.2.....	46
29. Band combinations that produced a FR greater than 3 with band 1 represented by a blue dot and band two by a red dot. The blue line connects the two bands that produced the respective FR.....	47
30. Best Fisher Ratio achieved with respect to time for (a) all data sets from BFII and (b) only the data sets that produced fit parameters from the five-band radiometric model.....	488
31. Class 1 and 2 projected onto the Fisher line with their respective PDF for (a) all data sets from BFII and (b) only the data sets that produced fit parameters from the five-band radiometric model.	488
32. Top panel to bottom panel: FRs greater than 6 from the three-band search with band 1 represented in blue, band 2 represented in red and band 3 represented in green. The regions that produced high FR values are labeled as FR Spikes; The spectral emissivity of the fireball in black, H ₂ O in blue, CO ₂ in red, and the soot represented by a dashed grey line; The spectral transmittance of the atmosphere. The semi-transparent grey regions represent the areas where the FR spikes resided.	49
33. Top to bottom panel: Spectral emissivity of the fire ball in black and the soot emission in gray; spectral emissivity of H ₂ O; the spectral emissivity of CO ₂ ; spectral emissivity of CO; spectral emissivity HCl; spectral transmission of the atmosphere; Grey regions representing the three best bands from the three-band search with a zoomed in region showing the band placement overlaid on the respective atmospheric transmittance.	500
34. The center bandwidth placement from a refined three band search which reduced the band step size to 5cm ⁻¹ to identify more precise placement of band to achieve the best FR within the FR spike region. Band 1, 2, and 3 being labeled blue, red and green respectively.	51

Figure	Page
35. TNT intensities for each event within the three-band FR spike for (a) band 1,(b) band 2, (c) band 3. All three bands are highly correlated with each other.	52
36. ENE2 intensities for each event within the three-band FR spike for (a) band 1,(b) band 2, (c) band 3. All three bands are highly correlated with each other.	53
37. The TNT and ENE test case spectral signature overlaid on each other at $t=0.4s$ with the red line representing band 1, blue line representing band 2, and the green line representing band 3.	53
38. Intensities from each bands are summed on the fisher line over time using the projection vector that achieved a $FR=41$	54
39. FR versus time using the best bands selected from the three-band search.	55
40. The orthonormal components from the best three bands using the BFII spectral data to derive integrated intensities that produced a $FR=41.3$ between TNT described by the red lines and ENE represented by a blue lines for (a) band 1 (b) band 2 (c) band 3	56
41. The orthonormal components from the best three bands using the model's spectrum to derive an integrated intensity which produced a $FR=5.5$ between TNT, described by the red lines, and ENE, represented by a blue lines, for (a) band 1 (b) band 2 (c) band 3.	57
42. Interferogram from the MR-154 during the BFII collection observing a detonation out of since with the intensity calculation.	65

List of Tables

Table	Page
1. Listing of the total number of different size and type of HE detonations during BFII and the number of them that were successfully observed.	5
2. Relative amounts of atomic species present within the different explosive types normalized to Carbon with a relative oxygen ratio required for complete combustion [1].....	5
4. Common radiometric variables and their definitions [1]	15
5. The relative stoichiometry for each HE type used in BFII [1].....	35
6. Computational times required to complete each search routine for the 2, 3, 4 and 5 band combinations.	45
7. Max fisher ratio achieved from the multiband search using two data sets; one including all data observations from BFII and the seconds only containing the data sets that were able to produce fit parameters for the five-band radiometric model.	45
8. Results from the leave one out test examining three-band FR spike from observed	52
9. Table showing the corrected times of the data and the start, end and delta in seconds of each observed event and whether or not it was used in the analysis.	65

ADVANCED RADIOMETRY FOR HIGH EXPLOSIVE FIREBALL DISCRIMINATION

I. Introduction

Explosives have been a topic of vigorous study since the first discovery of black powder. Researchers have explored several aspects of explosives to include increasing yield, lethality, developing precision charges, detection and exploitation of these devices, both pre and post detonation. The rise of improvised explosive devices (IED) being used in modern warfare today has inspired a flurry of new research within the fields of pre-detonation detection and post-detonation identification to help counter the threat of these potentially deadly devices.

Pre-detonation detection has dominated the explosive research community as it is applicable to both the civilian and military community and more importantly can save lives. A major catalyst to this research continues to be the maturing technology of terahertz frequencies. Within the terahertz (THz) spectrum most common high explosive (HE) materials such as Tri-nitro-toluene (TNT), RDX, HMX, etc, have a unique absorption cross section making them vulnerable to detection [1]. THz frequencies also have the advantage of penetrating through clothing and other common dielectric materials making it an ideal technology for standoff detection [2]. While the importance of pre-detonation is not questioned, with today's current technology it is essentially impossible and inconceivable to detect every explosive device before a potentially lethal detonation making explosive forensics essential.

Knowledge of key HE characteristics, such as its chemical composition and size, could provide critical insight about the perpetrator and potentially lead to his capture. Understanding if the device was constructed from readily made materials, such as ammonia nitrates, or military grade explosive materials provide fundamental clues to the culprit's sophistication and resources available to them. By identifying the size or chemical make up of the HE could tip off investigators to look for large orders of materials required to build the explosive in question [1]. Gas chromatography and mass spectrometry analysis can be

performed on samples collected from the scene at a remote laboratory. This requires on site collection, transportation and analysis of the samples from a potentially dangerous area. Throughout all of the ongoing research concerning explosives identification one aspect has gone relatively overlooked and that is the fundamental understanding and characterization of the electro-optical (EO) signature resulting from a HE fireball.

One method currently being researched to identify the characteristics of an explosive device includes using laser-based spectroscopy also known as active spectroscopy. This is a very precise method of detecting different chemical species present within the HE fireball [3]. The main drawback to this method is that prior knowledge is required of the where the detonation will occur which is almost impossible in today's hostile environment. A passive sensor could possibly meet this requirement, as it is more conceivable to be observing an area and not at an exact location and time. To develop a passive sensor to accomplish this an EO band must be chosen that is ideal for HE detonation discrimination. Infrared (IR) is an obvious choice, not only because it is a mature technology, but also because the IR spectrum encompasses several well understood emission regions, such as H₂O and CO₂, that are could be used for characterization.

Over the past decade the remote sensing group at the Air Force institute of Technology (AFIT) has collaborated with several ground-truth teams to collect a wide variety of robust data sets for several types of transient combustion events. The event types include explosive detonations, artillery and small arms muzzle flashes, and rocket plumes with all collections focusing within the EO spectrum. From these data sets, AFIT developed a simple phenomenological model for characterizing high explosive (HE) properties from their temporally resolved infrared combustion spectra. This was done by treating the fireball as a source in local thermodynamic equilibrium and describing the emission as Planckian blackbody radiation modified by a spectral emissivity and attenuated by an atmospheric transmittance profile. The spectral emissivity depends on the fireball temperature and combustion by-product concentrations (primarily soot, water, and carbon dioxide). The model reduces spectral data dimensionality to five parameters, which are useful in discriminating among various types of HEs, as demonstrated using time-resolved spectra collected

from TNT and a class of enhanced novel explosives (ENEs) in the Brilliant Flash II (BFII) field experiment [1].

This process of reducing the required amount of data to still achieve discrimination could be beneficial for anyone interested in HE fireball classification. It has been shown that HE fireball discrimination is possible with a resolved spectral sample [1] and this work will attempt to answer if discrimination still possible from a source with less spectral precision. This concept was a direct result of the examining the previous phenomenology based HE fireball model defined by five physical fit parameters. If several banded radiometers could be individually tuned to collect the required information to describe these features it could be possible to successfully discriminate HE fireball signatures without collecting a resolved spectrum. Radiometers are an extremely robust and a well-understood method of collection. Additionally radiometers have the ability to collect at very high acquisition rate, which could provide an additional temporal understanding of these EO signatures.

This study investigates the feasibility of using banded radiometers to derive the five key features required to characterize the emissions of a HE fireball. The radiometric intensity is estimated by integrating over previously collected spectra from the BFII experiments within the MWIR. By selecting a proper combination of band it is later demonstrated that the comparable temperatures and by-product concentrations could be estimated from these intensities using a spectrally integrated form of the fireball model. Fisher linear discrimination (FLD) is used as a measure of separation capability.

If the user does not have the resources to employ five bands or if one band fails to collect any information presents the problem of attempting HE fireball discrimination with fewer than five bands. It's not uncommon for an instrument to fail or be miss aligned leaving the user with a reduced number of bands. Also considering the unpredictable nature of hostile explosives, ensuring the proper placement of the sensor to collect an unknown event can quickly become a daunting logistical problem. With this in mind, even if there were five bands available to observe the area of interest it is conceivable that not all of your collection platforms would be tasked on the same target. This make the problem of performing characterization with fewer than five bands a very real and important problem. To investigate the potential us using fewer than five bands for classification, a search is performed across the entire collected spectrum

to identify the best band combination for HE detonation characterization with a reduced number of bands. Similar to the five-band radiometric model FLD is employed as a measure of discrimination potential. Due to the limited amount of collections available a strong statistical analysis of the data can not be performed.

1.1 Document Preview

Chapter one includes a brief overview of the background leading up to this problem to provide the reader with a foundation to better understand the problem at hand. This covers a basic overview on radiometry and the radiometric transfer process. The data collection from BFII is also described with the instrumentation used for collection. The work performed at AFIT by Dills and Gross discussed with a focus of the phenomenological spectral model developed by Gross to perform HE discrimination. Chapter two discusses the methods used to derive the five-band radiometric model and an explanation of band placement. An overview is provided on interpreting the derived intensities into the five fit parameters to drive the model. A revised radiometric model is also derived to account for some of the deficiencies encountered from the first attempt. Following this a description of the performance of using a fewer than five bands to perform discrimination and identifies band combinations that that yielded the best results. The five-band radiometric model was shown to be a feasible method to perform classification. The optimal band selections when using fewer than five bands is provided and highlights some regions with high classification potential that were previously unexamined. This is followed by a discussion of how these results are interpreted and recommendations for future work.

II. Background

2.1 Experimental Data

The foundation of this work is based upon the joint efforts of AFIT's Remote sensing group along with other collaborations with the purpose to observe and collect information for of HE fireball detonations. The collections from BFII, which was designed to collect electro-optical signals with the purpose of discriminating between ENE and TNT, were examined for this study [3]. This test took place from 2-14 June 2003 in the Utah test and Training Range. The different explosive sizes observed were uncased 10, 50, 100 and 1000kg ENE and TNT ignited with a 10% relative sized C-4 explosive charge. 44 detonations took place with 40 of them being successfully observed. The number of repetitions for similar events was very small which makes a robust statistical exploration of the data difficult. The collection summary is provided in Table 1. In addition to this, several of the ENEs were modified with the addition of booster materials to increase the combustion process totaling 5 variations of ENE detonations observed with their relative stoichiometry seen in Table 2. The data was recorded under optimal atmospheric conditions with relative low humidity and zero precipitation at an elevated location 3.26 km from the detonations with the

Table 1. Listing of the total number of different size and type of HE detonations during BFII and the number of them that were successfully observed.

HE	10 kg	50 kg	100 kg	1000 kg
TNT	4/4	4/5	2/3	1/1
ENE0A	1/1	0/0	0/0	0/0
ENE0B	0/0	4/4	2/2	0/0
ENE1	1/1	3/4	3/3	1/1
ENE2	1/1	3/4	2/2	1/1
ENE2B	0/0	4/4	1/1	1/1

Table 2. Relative amounts of atomic species present within the different explosive types normalized to Carbon with a relative oxygen ratio required for complete combustion [1]

HE	C	H	N	O	Al	Oxygen Ratio
TNT	1.00	0.79	0.48	0.89	0.00	0.370
ENE0A	1.00	24.02	12.36	17.90	4.08	0.89
ENE0B	1.00	21.26	10.99	15.83	6.12	0.726
ENE1	1.00	6.74	2.62	4.26	3.76	0.388
ENE2A	1.00	5.84	2.49	4.05	3.57	0.394
ENE2B	1.00	6.71	2.93	4.71	2.96	0.484

viewing geometry seen in Figure 1 [1]. The TNT and ENE variations HE detonations occurred in a mixed order to minimize the effect the changes in the climate would have on data. Measurements for the time (date time-group DTG based from Zulu), temperature (C), pressure (in-Hg), and relative humidity (%) were collected for each event displayed in Table 3 for all 44 detonations.

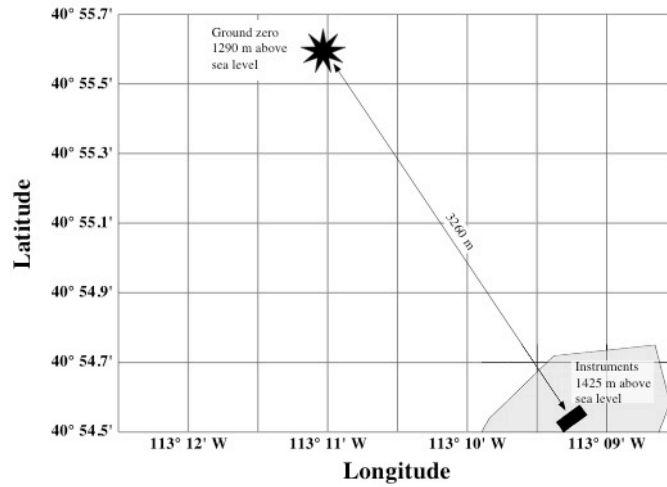


Figure 1. Viewing geometry of the sensor suite with respect to the detonation site during BFII [1].

Table 3. Climate observations for the BFII detonations

Event #	Test Article	DTG (Z)	Temp (deg C)	Press (in-Hg)	RH (%)
1	TNT-10	36312.75296	25	25.3	21
2	ENE0A-10	36312.81801	27	25.56	16
3	ENE1-10	36312.85586	27	25.26	16
4	ENE2A-10	36312.904	29	25.25	13.2
5	ENE1-50	36312.94127	29	25.22	14.9
6	ENE1-50	36312.97917	29	25.22	13.3
7	TNT-10	36313.01105	29	25.21	12.8
8	TNT-50	36313.75226	23	25.33	12
9	ENE1-50	36313.78744	23	25.31	9.2
10	ENE1-50	36313.83108	23	25.29	7.5
11	ENE2A-50	36313.87159	26	25.28	6.4
12	ENE2A-50	36313.93059	31	25.26	7.4
13	ENE0B-50	36313.9599	33	25.22	6.3
14	ENE0B-50	36313.99288	30	25.19	5.7
15	TNT-10	36314.03756	31	25.19	6.6

Event #	Test Article	DTG (Z)	Temp	Press	RH
16	TNT-100	36314.75343	21	25.31	19
17	ENE0B-50	36314.78676	23	25.3	18.1
18	ENE0B-50	36314.84116	24	25.29	15.3
19	ENE2A-50	36314.93961	27	25.27	12.2
20	ENE2A-50	36314.97675	26	25.26	12.5
21	TNT-10	36315.00638	27	25.26	12.7
22	ENE1-100	36315.74081	20	25.39	20.4
23	ENE1-100	36315.7866	22	25.38	16.4
24	TNT-50	36316.81524	24	25.38	14
25	TNT-50	36316.73971	24.3	25.31	18
26	ENE0B-100	36316.77443	25.6	25.29	16.4
27	ENE0B-100	36316.80869	26.5	25.29	13.3
28	ENE2A-100	36316.84289	27	25.28	11.9
29	ENE2A-100	36316.8775	28.8	25.26	8.7
30	ENE1-100	36316.91934	29.6	25.23	9
31	TNT-50	36316.95829	30.1	25.23	8.6
32	TNT-1000	36320.74594	30.6	25.13	14.1
33	ENE2A-1000	36320.97279	26.5	25.1	22.1
34	TNT-100	36321.74245	25.2	25.17	17.6
35	ENE1-1000	36321.79875	27.2	25.16	10.3
36	TNT-100	36322.7355	29.2	25.15	18
37	ENE2B-1000	36322.77317	28	25.14	18.3
38	ENE2B-100	36322.81304	27.7	25.13	16.8
39	ENE2B-50	36322.84024	29.1	25.13	15
40	TNT-50	36323.70898	23.6	25.24	29.2
41	ENE2B-50	36323.73757	25.1	25.24	25.7
42	ENE2B-50	36323.76159	25.3	25.25	24.5
43	ENE2B-50	36323.78521	28.4	25.25	19.4
44	TNT-50	36323.81009	28	25.24	18.8

The primary instruments used were two Fourier Transform Spectrometers (FTS) and one radiometer. The decision to implement an FTS as the principal instrument to observe the spectrum of HE fireballs was made due to it being a mature proven technology, having rugged field deployable instruments readily available, and advantages over other forms of spectroscopy that include throughput and multiplex [4]. The main disadvantage in using an FTS for HE fireball exploitation is that these short-lived events push the FTS to its limitations of collecting usable data [1] because the scene is changing faster than the acquisition rate of the instrumentation. To ensure the data collected was well behaved, it was compared

against another FTS that had a faster acquisition rate, and a radiometer and was found to have a high correlation with each other, which verified the integrity of the collections.

Fourier transform spectroscopy is a well-developed field of study, dating back to Michelson's interferometer in 1887. Information on the basic operation of interferometers can be found in works by [5,6,7]; basic knowledge of the mechanics of interferometers will be assumed here. The raw output of the interferometer is an interferogram seen in Figure 2, which contains the input signal as a function of optical path difference. A Fourier transform is performed on the interferogram to transform the input from the time domain to the frequency domain. With current FTS collection methods there is an inherent trade off in the collection of information with respect to spectral and temporal resolution. Using a passive FTS detector with highly resolved spectrum results in a poor temporal resolution of the source. Temporal characteristics or changes to the fireballs chemical evolution that occur faster than acquisition rate of the instrument will be missed which is an inherent limitation of using an FTS to collect highly transient events.

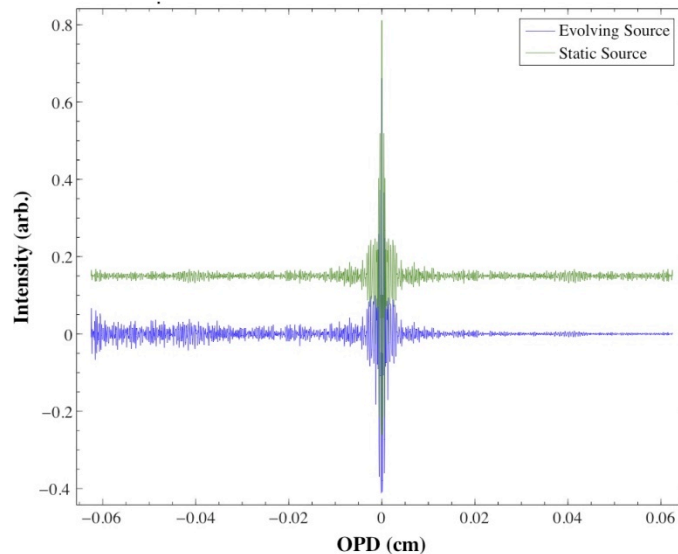


Figure 2. Two interferogram overlaid showing the statics source, on top, in green and the evolving source below in blue with scene change artifacts present in the signal [1]

The instrumentations software from the FTS commonly processes the interferogram into a usable spectrum with the assumption that the event observed is static and not transient. This not being the case

gives rise to the possibility of artifacts being introduced into the spectrum because of the transient nature of the source, which is commonly referred to as scene change artifacts (SCA) also seen in Figure 2. Fortunately the impact on the real component of the data from of SCAs is relatively minor [1,8].

The spectrometers used were the ABB/Bomem MR-154 and an ABB/Bomem MR-354 FTS. Both were fitted with slightly different Indium Antimonide (InSb) detectors and similar Mercury-cadmium-telluride (MCT) detectors. Calibrations were performed as indicated in Dills' test report [9] and used black bodies placed approximately 15m away from the MR-154 at temperatures between 900-1000k. Due to a calibration issue with the MCT detectors, explained in further detail in Gross' dissertation [1], the MCT was not used which limited the usable data to a spectral range between 2000-7000 cm^{-1} . MR-154 and MR-354 observed the detonations at 4 cm^{-1} at 8 Hz and 4 cm^{-1} at 34 Hz respectively. To maximize the signal to noise ratio (SNR) for the MR-154 the gain and other settings were adjusted for each observation, but resulted in some of the observed events saturating the detector and were excluded from analysis further reducing the usable data set.

The four-channel radiator employed fielded by ATK-MRC was equipped with 4 InSb detectors fitted with several band pass filters and optical density filters that operated at 2KHz but was later downsampled to 200Hz to improve the signal to noise level (SNR). A sample data cube taken from the MR-154 is seen in Figure 3 that has been reduced to 16 cm^{-1} to improve readability [1]. In addition to these instruments, several other instruments were employed during this test and are described as follows. A Princeton Instruments 0.25m grating spectrometer was used to collect information in the visible spectrum. The Indigo Systems Alpha NIR camera using an InGaAs focal plane array at 30 Hz observed in the near infrared spectrum and a Canon XL-1 3 chip video camera provided audio-visual documentation of the test and used for quantitative analysis. In addition to these, several other instruments were used collect meteorological data that were used to later calculate and account for the atmospheric transmittance profiles which modify the source spectrum.

To ensure the data collection was robust the MR-154, MR-354, and radiometer were all compared to each other. This was done by integrating over the band pass filters used in the radiometer on the

spectrum detected by the spectrometers. This compared their apparent intensity signatures of the detonations. While some of the data correlated well, the MR-354 and the radiometer had a very close agreement in their observations and considered very reliable. The data from the MR-354 and radiometer were then used to correct for the scale discrepancies observed in the MR-154. This ensured that the MR-

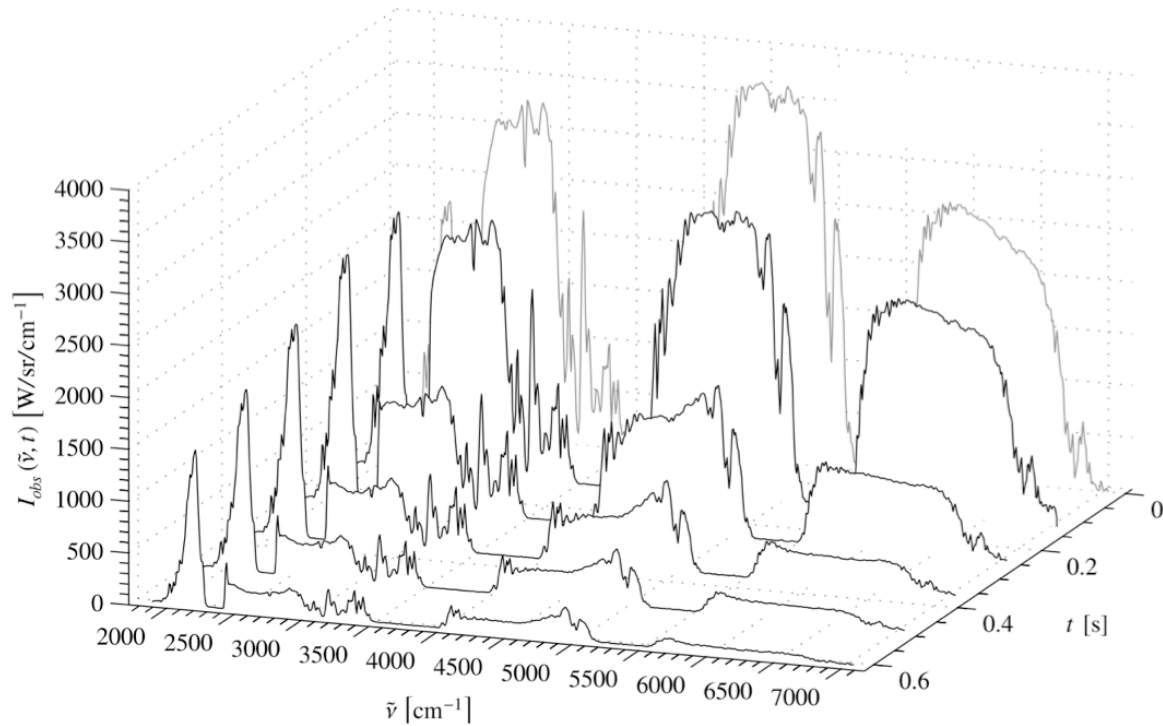


Figure 3. Data cube of apparent intensity from a typical munitions detonation with a degraded spectral resolution of 16cm^{-1} , reduced from 4cm^{-1} , and a temporal resolution of 8 Hz respectively [1].

154 was scaled correctly because it had a superior SNR to the MR-354, which lacked a cold source reference like the MR-154. Figure 4 shows an ideal case where both FTS instruments and the radiometer were in high agreement with each other [1].

2.2 Dills' Research Overview

Dills, an AFIT graduate performed some of the initial research on the data set briefly described above. The focus of Dills' work investigated the discrimination potential of extracting features from a broad spectrum of video imagery using statistical methods as a benchmark. By reducing the imagery data

to 14 features allowed for an examination the discrimination ability of several temporal features such as the growth rate, time to peak, full half width max (FWHM) and the decay rate of the intensity. The Time to peak showed the highest potential for discrimination out of all the temporal variables examined.

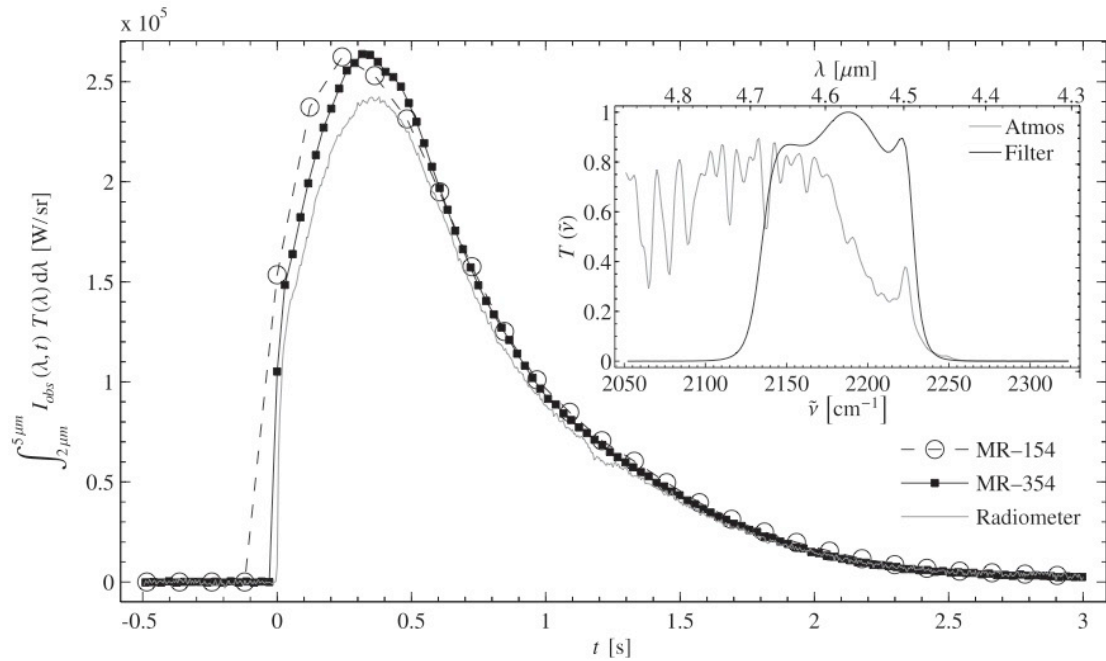


Figure 4. Comparison of absolute intensities collected by the MR-154, MR-354 and the radiometer for a detonation of a 100 kg ENE. The inserted plot shows the transmittance T of the used bandpass filter (black) used by the radiometer and the spectral ranged that was integrated over the transmittance of the atmosphere (grey) in that region for reference [1].

The statistical tool implemented to measure the discrimination potential was Fisher Linear Discrimination (FLD), with a full mathematical explanation is provided in the following reference [10, 11]. The Fisher Ratio (FR), is a measure of the FLD that essentially squares the difference of the means of each data class and divides that by the sum of their variances which is used as a benchmark for discrimination capability. Equation 1 shows how the FR is computed where D is the number of features describing each class, \bar{x} is the mean of the respective class, C is the number of classes, and σ^2 is the variance.

$$FR = \frac{\frac{1}{D} \sum_{i \neq j} (\bar{x}_i - \bar{x}_j)^2}{\frac{1}{C} \sum_k \sigma_k^2} \quad (1)$$

An example of the FLD is seen in Figure 5 where three classes, A, B, and C are projected onto the Fisher Line from feature F_1 and F_2 . A single feature is unable to separate all three classes as F_1 can separate class A from B and C, but cannot split Class B from C. The same is true for F_2 where it can separate class A and B from C, but can not distinguish A from B. Classification is achieved by using both features and projecting each class onto the Fisher Line using a linear combination of these features to in a way that maximizes the separation between all three classes. The FR is a measure of this separation between classes. Looking at Figure 5 one can see how the FR between from class A and B would be much smaller than the FR from class A and C, as class A and C have a larger separation between them with no overlap on the distribution projected onto the Fisher Line.

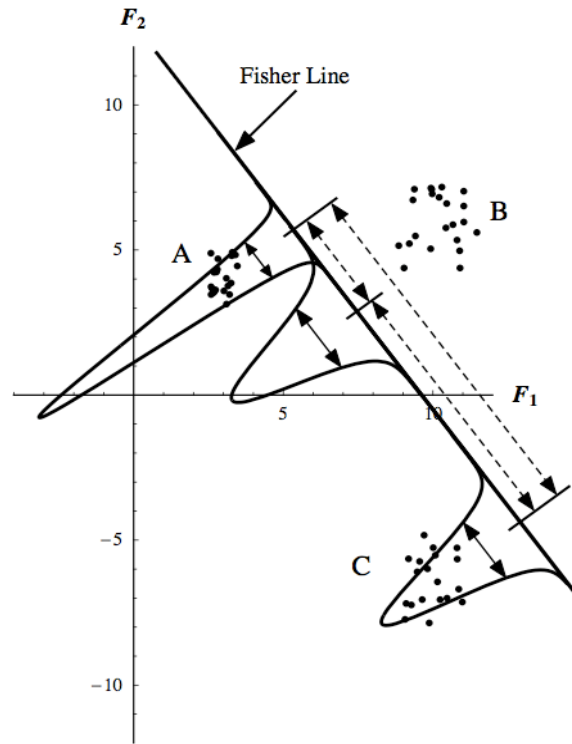


Figure 5. Three classes, A, B and C projected onto a Fisher Line calculated from feature F_1 and F_2 . A probability distribution functions is shown projected over the respective data points from each class from the Fisher Line. Each class variance is displayed by a solid line and the distance between the mean of each class is also indicated by a dashed line. [12]

To provide better feel of what an actual FR number actually implies with respect to classification capability, two examples are provided below. The first example, seen in Figure 6, shows two classes of data described by two features. Applying the FLD finds the best linear combinations from the two features to maximize the separation between the two classes. There is no linear combination that provides a good separation between the two classes and this is indicated by a $FR=4$. The overlapping probability distribution functions (PDF) from each class provide a visual indication that the data is not well separated. The second example, seen in Figure 7, depicts two data sets that can be highly separated through FLD.

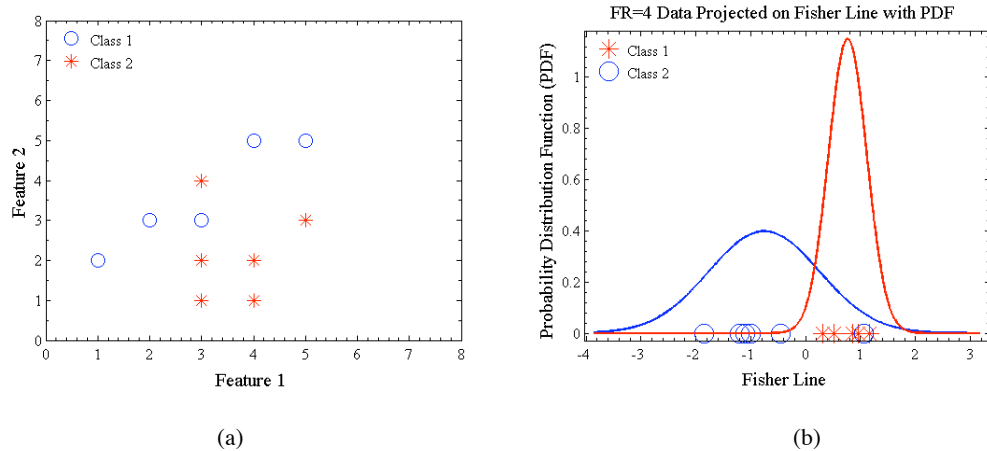


Figure 6. (a) Two classes of data described by two features with a $FR=4$; (b) Both classes of data projected on to the fisher line from FLD with their respective PDF and a $FR=4$.

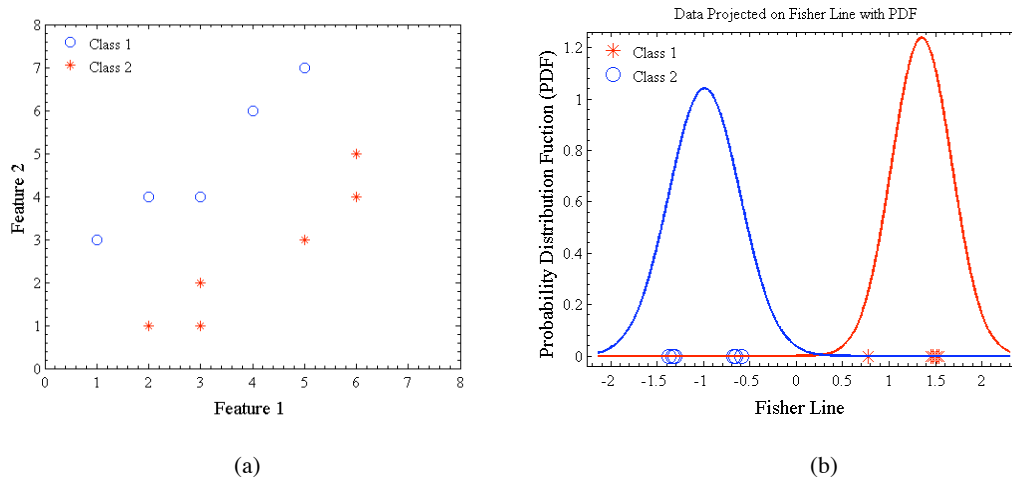


Figure 7. (a) Two classes of data described by two features with a $FR=43$; (b) Both classes of data projected on to the fisher line from FLD with their respective PDF and a $FR=43$.

The respective PDFs do not overlap and can be easily separated which produce a FR=43. The study also combined some of the IR, visible and near visible imagery collections, which did not provide an increased classification potential. The best feature identified within the IR collections was determined to be the time-integrated intensity of the fireball [3].

2.3 Gross' Research Overview

Performing concurrent work at AFIT with Dills, Gross' research ultimately provides the foundation of this study. While Dills' performed a highly statistical approach towards discrimination, Gross attempted to map the spectral emissions to a simplified real physical model to identify the best spectral features present for classification and discrimination. The following is a brief primer on radiometry followed by a summary describing his physics based fireball model and results from his research [1].

The fundamental physics behind this study lies centered between radiometry and spectrometry.

Radiometry is used to determine the effects on the photon emission from a source as it propagates to the detector. Common variables and their units used in radiometry are seen in Table 4. The raw measurement that would theoretically occur at the source, unaltered from any of its surroundings is commonly referred, as I_{src} , the source intensity. The source intensity is very difficult to directly collect and in the case of HEs it would be impractical to place a detector within the destructive radius of explosion. The only way to characterize the source intensity is to understand the surrounding environment and how it manipulates the signal from the source to the detector. The signal that reaches the detector is called the apparent intensity, I_a . To calculate the source intensity from the apparent intensity there are several factors that need to be considered that include but are not limited to the background, transmission through the atmosphere, random photons from other sources, and losses plus noise from the detector. The radiometric transmission is depicted as a simple flow chart below in Figure 8, which describes the following five areas under consideration for the transfer model:

Table 4. Common radiometric variables and their definitions [1]

Symbol	Name	Units
A	area	cm^2
R	length	cm
θ	linear angle	rad
Ω	solid angle	sr
ϕ	flux	W
L	radiance	$\text{W}/(\text{cm}^2 \text{ sr})$
I	intensity	W/sr
E	irradiance	W/cm^2
B	Planck distribution	$\text{W}/(\text{cm}^2 \text{ sr cm}^{-1})$

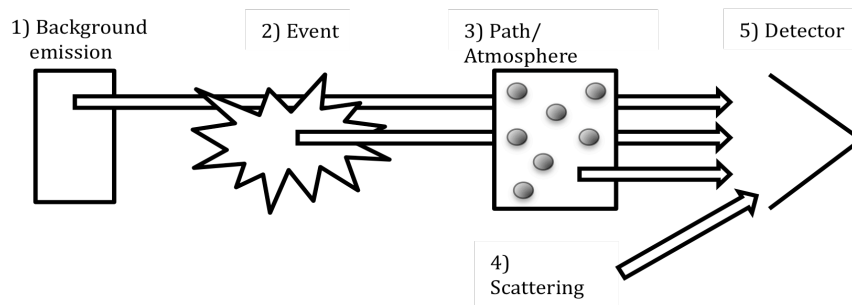


Figure 8. Simplified radiometric transmission showing typical sources of noise and losses.

- 1) Emission present from the background is comprised of multiple objects and temperatures that do not act as perfect radiators but as an absorber, emitter and reflector of photons. The signal propagating through the fireball is further altered by transmission characteristics of itself.
- 2) Every object that radiates acts as both an emitter and absorber. Emissions from the background that reach the event are effected by both of these aspects resulting further absorption or stimulated emission. The optical thickness and transmission properties of the event will alter the signal from the background non-uniformly in the spectrum.
- 3) The combined signal from the background and source now pass through a spectral transmission of the atmosphere. The source and background emissions are attenuated in a spectrally dependent manner, which depends on the path length and the absorbing gas concentrations present. Additionally the path itself acts as an emitter, which technically adds to the overall signal, but its contribution is small enough where it can typically be ignored.

- 4) Scattering occurs when photons are redirected which alters their path and can occur at any stage of the radiometric transfer process, introducing photons from completely unwanted sources.
- 5) Inherent losses are present within the collection optics and detection system.

The sum of all of the sources, losses and transmission functions briefly described above gives the apparent intensity. A detailed derivation of the radiometric transfer model is provided in Gross' Dissertation [1]. While this is by no means complete, it provides a general overview of some of the complexities of understanding the radiometric transfer model and the considerations that must be taken to obtain the source intensity. The experimental data will now be discussed addressing several of the issues and problems stated above.

The physics based model was derived from the infrared spectrum collected by the MR-154. Using a basic understanding of the chemical make-up of TNT and ENE and the combustion process, five primary emissions studied included: H₂O, CO, CO₂, HCl, and the soot concentration. Since the concentrations of TNT and ENE were known, their individual molecular emissions could be modeled using the spectral line-by-line HITRAN database. To implement this and still keep the model simple several approximations to the radiometric transfer model had to be made. The first was to assume the fireball could be described as a system in local thermal equilibrium. Also, that the emission source is comprised of a uniform temperature and originates from a uniform cube normal to the detector. This greatly simplifies the radiometric transfer model, as knowledge of the temperature distribution within the fireball is unknown. Additionally by using a uniform temperature for all the sources allows for the use of a simple Planckian model greatly reducing the computational complexity of the problem. This can be expressed as:

$$I(\tilde{\nu}) = \tau(\tilde{\nu})I_{src}(\tilde{\nu}) \quad (2)$$

$$I(\tilde{\nu}, t) = \tau(\tilde{\nu})\epsilon A(t)B(\tilde{\nu}, T(t)) \quad (3)$$

where τ represents the atmospheric attenuation, ϵ is the frequency-dependent emissivity, A is the Area of the fireball, $\tilde{\nu}$ is the wave number in cm⁻¹, t is time in seconds and B is the Planckian distributions at a

temperature T in Kelvin [1]. The atmospheric transmittance profile was calculated using a line-by-line-radiative-transfer-model (LBLRTM) [13]. Fitting this to the BFII data and comparing the Planckian blackbody intensity (I_{plk}), modeled intensity (I_{mdl}), and the source intensity (I_{src}) is seen in Figure 9, which also shows the known emitters and transmission within the atmosphere. Any photon scattering that occurs or self-emission from the estimated 300K background during the collection is also ignored. The temperatures from the fireball are so much larger than other temperatures present. Because the Stefan-Boltzmann law dependent upon temperature makes the emission from the fireball dominates all other radiative sources. This is where the total energy radiated by a blackbody can be described by the Stefan-Boltzmann constant, $\sigma=5.6703 \times 10^{-8}$ watt/m²K⁴, the temperature T in Kelvin, P as power in watts, and A

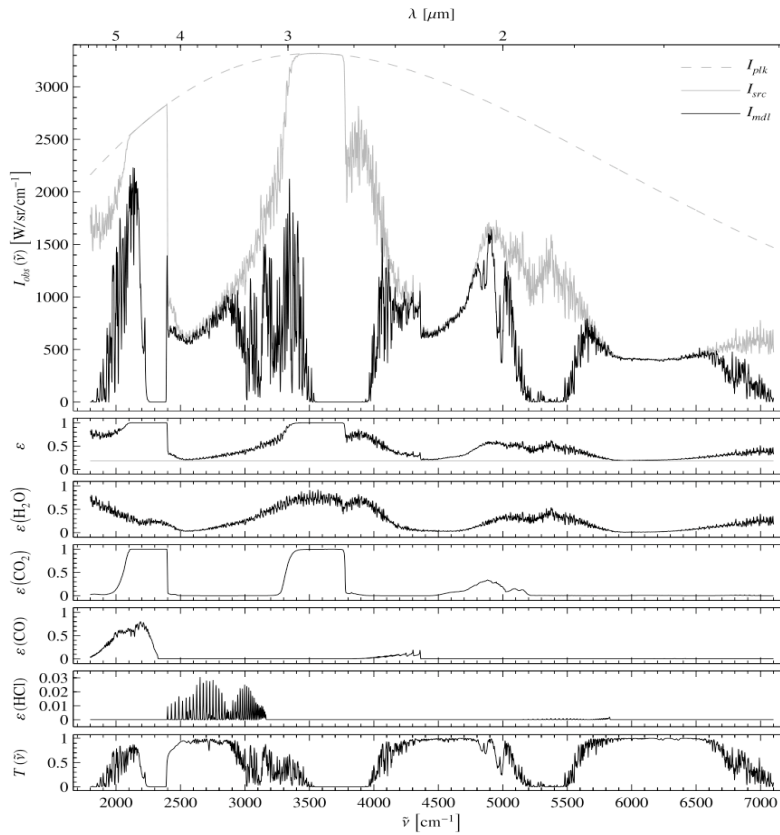


Figure 9. Top to bottom Panel: A comparative Planckian blackbody signature, the source and modeled intensity/The emissivity of the atmosphere/emissive spectral regions of H₂O present in the atmosphere/emissive spectral regions of CO₂ in the atmosphere/emissive spectral regions of CO in the atmosphere/ emissive spectral regions of HCl in the atmosphere/Transmittance of the atmosphere as a function of wavenumber. [1]

representing the area in m^2 and seen in equation 4 [14]. To simplify calculation of the required emissivity, the reflection component is assumed to be zero. This yields equation 5 where κ_p is the soot absorption coefficient in cm^{-1} , x is the radius, σ_i is the Boltzmann-weighted absorption cross-section, and ξ_i are the selective radiative gas emitters in cm^{-3} [1,14].

$$\frac{P}{A} = \sigma T^4 J / m^2 s \quad (4)$$

$$\varepsilon = 1 - e^{-\left(\kappa_p + \sum_i \sigma_i(\tilde{\nu}, T) \xi_i\right) x} \quad (5)$$

By combining these equations leads to the final equation 6, which models the source and apparent intensity.

$$I_{mdl}(\tilde{\nu}) = \tau_{atm}(\tilde{\nu}) x^2 \varepsilon(\tilde{\nu}; \kappa_p, \xi_i, T) B(\tilde{\nu}; T) \quad (6)$$

The apparent intensity model was then fit to the data. Through this fitting process it was found that six (with the exclusion of CO) main features were needed to accurately fit the model to the observed data. These were the size, temperature, soot, H_2O , CO_2 and HCl concentrations. Using these features the physics-based model was shown to closely match the observations from BFII. Immediate observations showed a direct correlation between the explosive type and peak temperature, where the ENE was typically larger than TNT. Additionally there appeared to be a correlation between explosive yield and the rate the temperature declined from the detected peak intensity, which is seen in Figure 10 [1].

Further discrimination was performed by examining the hydrogen to carbon ration between different explosives, which is related to the stoichiometry of the HEs. This proved to be a reliable tool to correctly identify TNT from and ENE emission spectrum. Using the Hydrogen to Carbon ration (HCR), a Fisher ratio of 17.5 was calculated which provided a distinct separation of the two explosive types. The results of a TNT and ENE HCR ratio is seen in Figure 11.

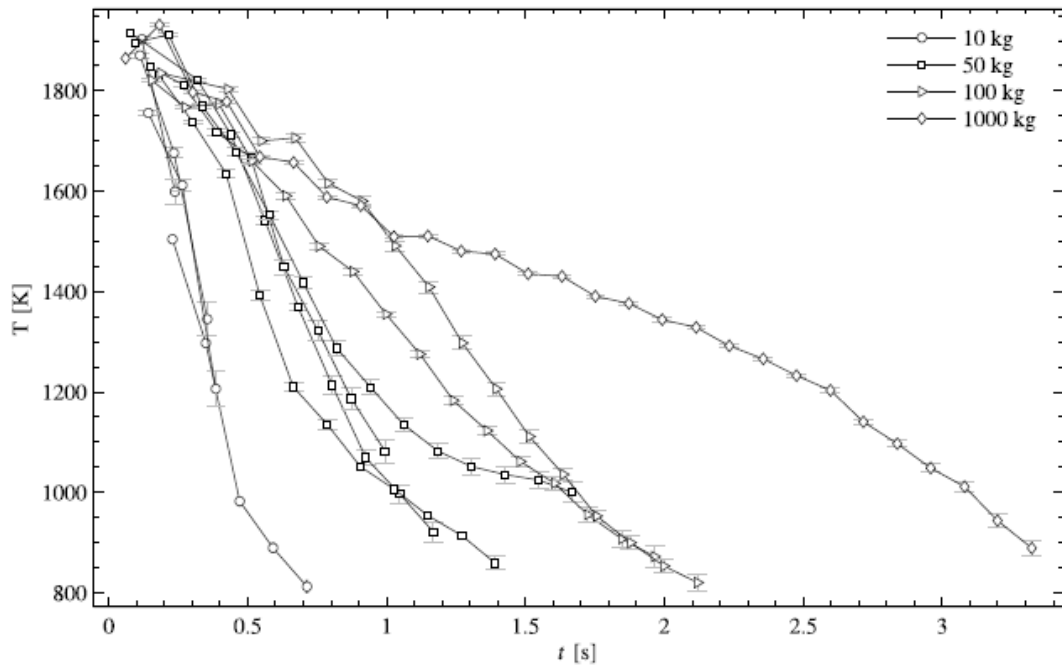


Figure 10. Temperature versus time curves obtained by fits to fireball spectra of 10 (o),50(square), 100(Δ), 1000(\diamond) kg charged of TNT. Error bars represent fit parameter uncertainties at the 95% confidence level [1].

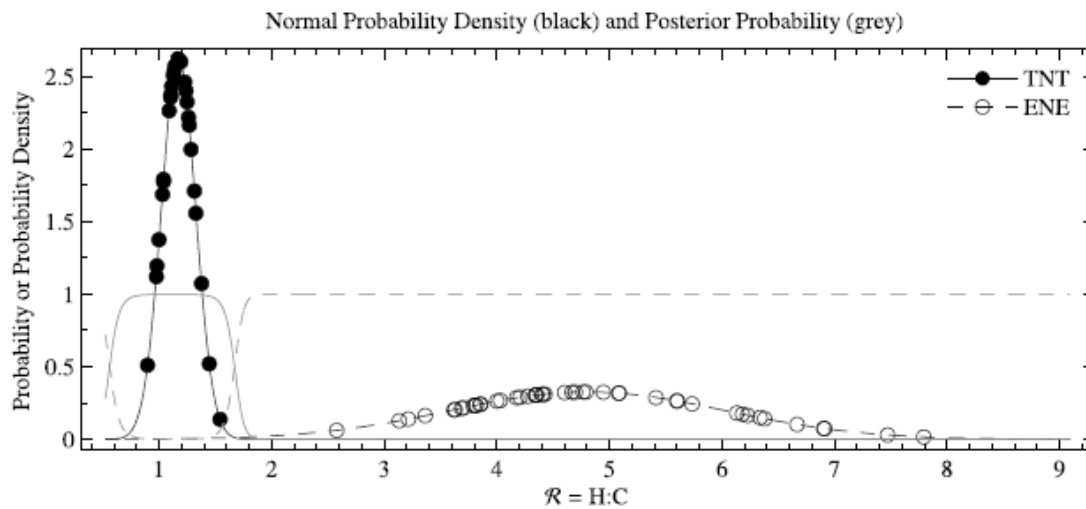


Figure 11. TNT (solid black) and ENE (dashed black) probability densities based on spectrally extracted R values and assuming a normal distribution. This distribution has a calculated fisher ratio of 17.5. [1]

This chapter briefly covered an overview on the radiometric transfer model and the required considerations to solve for the source intensity. The data collected from BFII was outlined along with

some of the characteristics of the collections. The previous research at AFIT was discussed focusing on the phenomenological based spectral model based upon the temperature, size and gas emissions from the fireball. The simplifications required to solve the radiometric transfer processes were discussed and supported by the results achieved by the model. The following section will discuss how this model is modified to use five radiometric bands in place of the spectrum. A description of how the five bands were selected and how the fit parameters were derived for the radiometric model are presented. Lastly a description of how the optimal bands were identified to perform discrimination when fewer than five bands were used.

III. Methodology

This section will describe the two methods implemented during this investigation to assess the feasibility of using radiometric bands for classification of HE fireballs. The first method replaces the spectral signature with five radiometric intensities interpreted into the five fit parameters features required for the Gross' fireball model to achieve classification. The second approach is to identify the best radiometric bands when fewer than five are present for analysis. To accomplish this, a systematic search over all combinations was examined through linear combination to achieve classification between two classes. Before these approaches are described, an examination of the data is provided. During this examination of the interferograms it was ascertained that the times associated with the FTS scans could be corrected to better match the actual time of first detection. A method was derived to temporally adjust the tagged times from the FTS and is explained in detail within the appendix. Following these corrections this chapter begins with an explanation of data set selection and exclusion methods to perform the desired analysis stated above. The process of using five integrated intensities to derive the five fit parameters this then presented. The chapter is concluded with a description of using a linear combination of fewer than five integrated radiometric intensities to perform discrimination.

3.1 Data Matching

To properly analyze the classification methods the data sets from BFII were examined to define which sets would be logical and beneficial to include in this study. The criteria to include an event required that it had a minimum of five temporally overlapping data points with the rest of the data. Each scan from the FTS was 0.121s, which set the minimum duration of an event at approximately 0.6s. This helped simplify the code and removed events that could possibly have a low SNR. This was also to reduce error present in the fitting algorithms described later, as the fitting implemented used variables from the preceding scan as the starting point. An algorithm was written to find the maximum overlap present between the data sets and the results are listed in the appendix in Table A1. This immediately removed all the 10kg events, which typically had only one or two data points, and some of the 50kg events from the BFII data set.

Several other events were identified to have little or no overlapping times with the rest of the data and were henceforth removed from analysis. This reduced the number of usable data sets from 38 to 28, further limiting the statistical confidence for the following analysis. Figure 12 shows the intensity vs. time for all the data sets circled that did not had fewer than 5 data point and did not to span the required time. Figure 13 is a depiction of the intensity vs. time with all the 10 kg events removed and highlighting the region with the maximum overlap within the data.

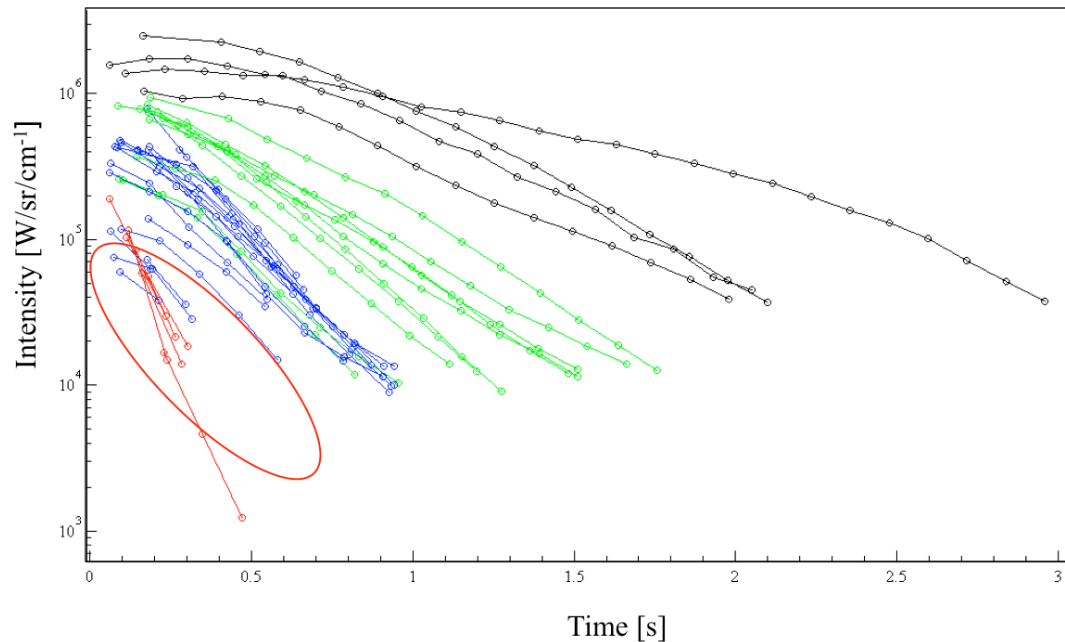


Figure 12. All of the data sets from BFII with the 10kg events in red, 50kg in blue, 100kg in green and the 1000kg in black. Events had fewer than 5 data points and were later removed.

3.2 Five Radiometric Bands

Achieving successful characterization of a HE fireball using a combination of banded radiometers, which replaced the rich information provided by a spectrometer is no trivial task. This requires priori knowledge of the source and of the atmospheric transfer function to ensure that the maximum amount of usable information can be extracted. Five primary fit parameters identified from the spectral model were correlated with spectral regions containing the required information for optimal band placement. Once these bands were identified, the derived intensity would be used to calculate the model's five fit parameters.

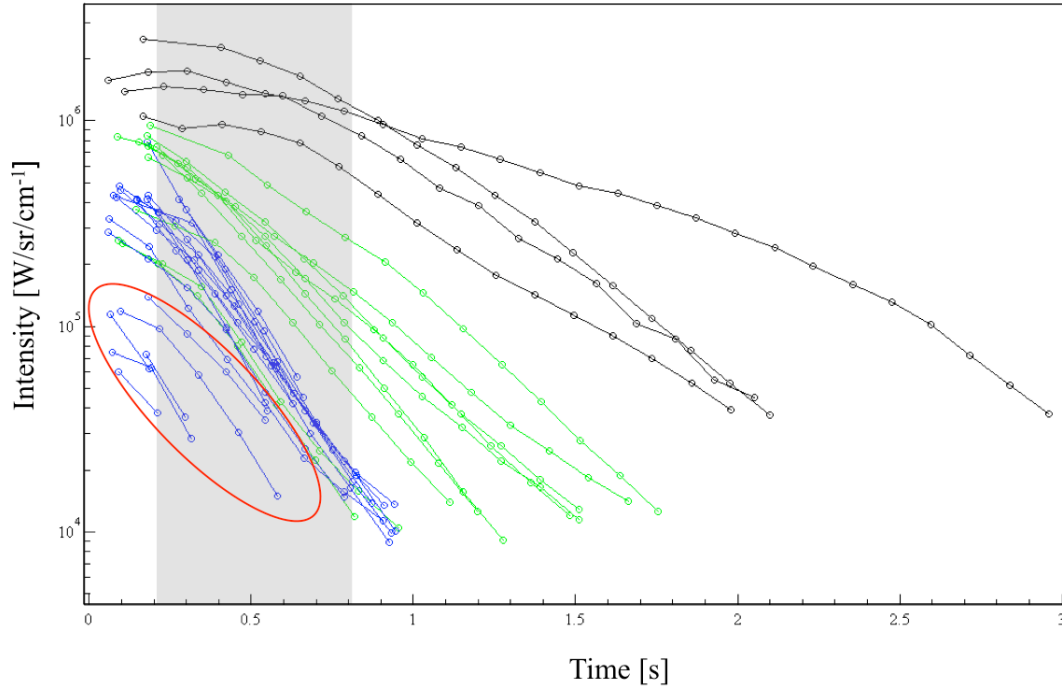


Figure 13. Show the 50kg events in blue, the 100kg events in green and the 1000kg events in black. The grey region shows the area of maximum overlap in the data where several of the 50kg events do not span and were removed from the data set for analysis.

By using five bands to solve for five parameters is mathematically similar to solving for five unknowns with five relevant equations. This is possible ensuring the following caveats are made.

- 1) Bands must be selected within a region where the desired feature exists
- 2) Feature must be observable and not fall on any atmospheric absorption regions
- 3) Without careful consideration of band placement and its physical relationship between the intensities may result in the actual physics deriving a trivial non-meaningful solution.
- 4) Any spectrum derived from a combination of intensities must be compared to the actual spectrum for validation

The fit parameters used are the fireball temperature, size, and the emissions from soot, H₂O and CO₂. The first band, placed at 2120-2280 cm⁻¹, was used to collect in a region that has an emissivity very close to one to be used later to derive the area of the fireball. The second and third band, respectively placed at 2530-2630 cm⁻¹ and 4750-5100 cm⁻¹, were selected due to the similar emissivity and little or no emission from CO₂ or H₂O. These two bands will primarily be used in the calculation of the temperature

and area. The fourth band, placed at 4480-4590 cm^{-1} , was selected over a region with very strong H_2O emissions to isolate its concentration in the spectrum. The fifth band, placed at 3885-4375 cm^{-1} , is selected to over an area with a high CO_2 emission to be used in solving for its concentration and the Hydrogen to Carbon Ratio (HCR). These band placements are depicted in Figure 14 by the semi transparent gray bars.

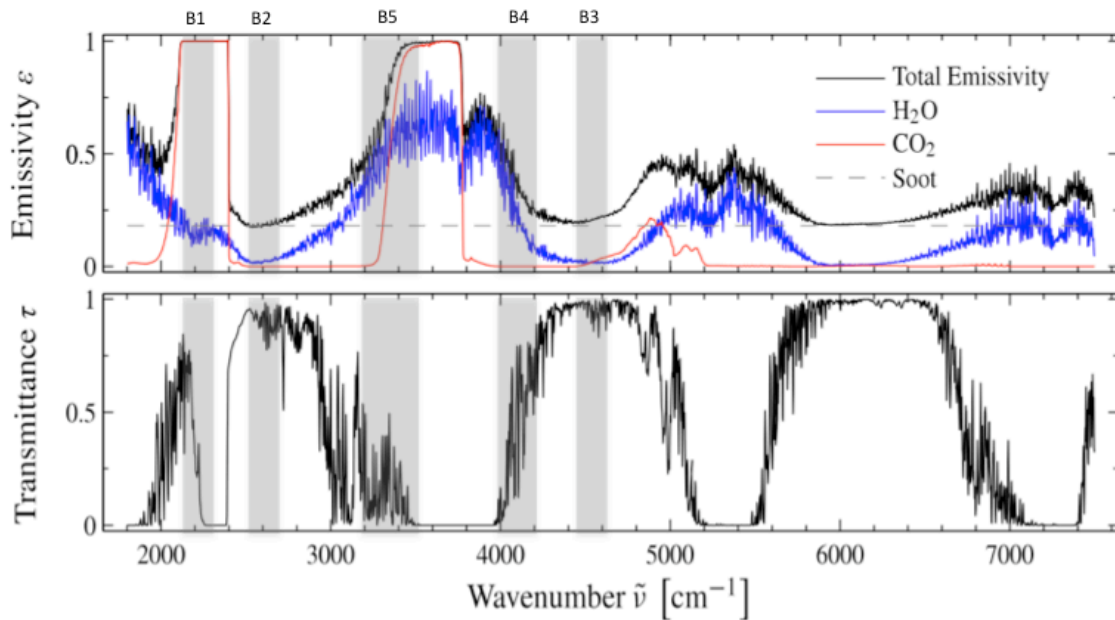


Figure 14. Top Panel: The H_2O , CO_2 , soot and total emissivity is shown spectrally. The gray regions indicate the band placement for the radiometric model. Bottom Panel: The spectral transmittance of the atmosphere with the grey regions indicating band placement for the radiometric model

Temperature.

Approximating the source as Planckian blackbody, with a uniform size and temperature, allows for a simple calculation to derive the fireball temperature. This process is commonly referred to as the color temperature of a black body. This is a temperature that best matches the spectral distribution of a blackbody source and requires measurements from at least two unique spectral regions. Additionally the observations must take place in a region with a low spectral emission and absorption from H_2O and CO_2 and with similar total emissivity. Color temperature is commonly referred to as a ratio of two exitances at two different wavelengths that are set equal to a ratio of two Planckian blackbody equations defined by a single temperature as seen in equation 7 [14]. Two regions that meet these criteria and were used are

centered near 2580 cm⁻¹ (B2) and 4600 cm⁻¹ (B3) as seen in Figure 14. Once the color temperature is solved for, the temperature and is input into one of the Planckian blackbody equations to solving for the emissive area (ϵA).

$$\frac{M(\nu_1)}{M(\nu_2)} = \frac{\nu_2^3 \left(e^{hc\nu_2/kT} \right)}{\nu_1^3 \left(e^{hc\nu_1/kT} \right)} \quad (7)$$

Area.

To separate area from the emissive area, ϵA , requires a band where the emissivity can be assumed to be one. While the spectral region centered near 3500cm⁻¹ exhibits an emissivity near one it is always right in the middle of a large atmospheric absorption band making it a poor choice as seen in Figure 14. This leaves the region centered at 2200cm⁻¹ (B3) that lies within a transmission region of the atmosphere as a viable option. Using the intensity from this region allows for the area to be solved for by dividing by already solved for emissive area (ϵA) by the emissivity (ϵ), which yield the area of the fireball.

Selective emitter concentrations and the HCR.

Solving for the individual molecule concentrations requires a detailed model to accurately represent the emissions from different excited molecules. Similar to the previous approaches in deriving fit parameters, an intimate understanding of the individual species emission and absorption regions is required. The two species also need to be isolated from other sources or and inaccurate intensity could be derived for by containing emissions from several substances. As seen in Figure 14, the H₂O emission is the easiest to isolate from the CO₂ emission regions. The region used to calculate the H₂O concentration is centered at 4100cm⁻¹ (B4) where there are no CO₂ emissions. Estimating the amount of H₂O present requires the utilization of the line-by-line radiometric transfer model (LBLRTM) code [1] to generate an emission spectrum to compare against the integrated intensities. Once the concentration of the H₂O is known, solving for the CO₂ concentrations becomes a simpler task as regions be can were both H₂O and CO₂ exist can be included. This is because the concentrations of H₂O is already known and can be removed from the region containing CO₂. The HCR is then derived from these two values as seen in equation 8.

$$\text{HCR} = (2 * \text{H}_2\text{O}) / \text{CO}_2 \quad (8)$$

3.3 Five band Summary

Understanding the band selection process provides the ability to derive the key features required for the model to emulate the observed EO emissions. Once the five fit parameters, temperature, area, soot, H₂O and CO₂ concentrations are solved for, a robust and thorough comparison between the generated spectrum created from the integrated intensities and observed spectrum is performed. In chapter 3 the results from the radiometric model are directly compared with those from the spectral model and the collected data. While this process was derived directly from an understanding of the physical model it should be noted that the method and band placement described may not be the optimal solution. A superior solution is still likely as there may be other bands that were not fully understood or exploited by the current spectral model. This is where a statistical approach could be used to verify this process and help identify other additional spectral features within the HE fireball emissions that remain unidentified.

3.4 Multi-band Search

When five bands are not available to derive the required fit parameters, the model becomes unbound. Since the model can no longer be used, the previous restrictions placed on mapping the spectral band to a model fit parameter is lifted. This opens an endless combination of spectral bands to be examined. By investigating previously ignored spectral regions may provide and insight in to new discrimination capabilities and could help bridge the knowledge gaps within the current spectral model. To accomplish this requires a systematic search across a large combination of spectral band combinations. Because of the low acquisition rate of the spectrometer, linear interpolation was performed between the intensity points to fill in the gaps between the collected data points. This provided a better correlation between the time and intensity when referencing multiple data collections to each other. This also provides an enhanced number of data points that can be compared by FLD. While linear interpolation was selected to be the method applied, it is understood that the actual nature of the intensity between data points may not actually be linear, but provided an adequate approximation. The data sets were then temporally compared to find the maximum number of collections that overlapped in time. FLD was then performed to find the

maximum FR to be used as a measure of discrimination potential for that band combination. The algorithm developed to accomplish this performs a search of the entire temporal region returning the maximum FR calculated, each bandwidth used for that FR, and the time that maximum occurred. To ensure the FLD algorithm developed worked correctly the results were verified using a known test data and an independently developed FLD code. The multi-band search was performed for three cases, which included a two, three, and four-band combination search over the MWIR spectrum. The five-band was excluded as the theoretical computational time greatly exceeded the timeline of this research. The four-band search was accomplished by breaking it up into sections over 17 computers running simultaneously. Because the possible combinations of bands are inherently infinite, some constraints had to be levied to ensure the search algorithm was computationally feasible. A fixed bandwidth of 100cm^{-1} implemented with a standard step size of 50cm^{-1} . This allowed for some overlap with each band shift to help to identify high areas of discrimination and reducing the number of iterations required for the search loop.

This section described some of the processes used to replace the spectral signature with radiometric bands to derive the features required for the Gross fireball model. A brief justification of band selection criteria was also described. The method used to compare and measure the utility of these bands for discrimination will be demonstrated using the FLD and the resulting FR. The data sets were then analyzed again to find the regions of maximum overlap with the purpose of using this temporal region for band comparison. A systematic multi-band search is performed over the collected EO spectrum without intuition of band placement. This search would rely on the statistical methods of the FLD and the FR to locate and identify the bands of interest. This resulted in some very unintuitive and unexpected findings that are described in the following chapter.

IV. Results

In the previous chapter the two methods were discussed to achieve classification between TNT and ENE HE fireballs; the five-band radiometric model and the multi-band search. This chapter will discuss the finding of these two methods and determine the feasibility of performing classification from a combinations of radiometric bands. First the five-radiometric bands interpreted into the five fit parameters for the spectral model will be discussed. The findings will show that while this method can be used to achieve discrimination between ENE and TNT HE fireballs, it does not accurately calculate the selective gas emitter concentrations. To correct for this, a revised radiometric model is presented. This revision reduced amount of error present in the original radiometric model and successfully produces all five fit parameters within a high level of agreement to the spectral model's results. Lastly the results from the multi-band search which used raw intensities in a linear combination to perform discrimination for two, three and four bands is presented. This uncovered a highly confined spectral region that indicated a very high classification potential from its FR. A description of this region, referred to as the FR spike, concludes this chapter.

4.1 Five-Band Radiometric Results

Using the methodology described in the previous chapter for band selection, the five fit parameters used in Gross' fireball model were derived from the integrated intensities for a majority of the data sets. The accuracy of these fit parameters with respect to the spectral results is presented later. Five data sets were unable to calculate a reasonable value for the model fit parameters. These five collections produced fit parameter values that were outside of the defined limits for the radiometric model. These bounds, based upon the spectral model's results, ensured that the fitting algorithm produced realistic values and did not produce a nonphysical solution. Because of this, these data sets were excluded from further analysis, further limiting the number of collections compared in this study. The problems encountered from these excluded data sets were likely from a low SNR present within the collections.

For the remaining data sets that were able to produce reasonable fit parameters describing the fireball's temperature, size, soot, H₂O and CO₂ concentrations created a good emission spectrum of the

fireball when input into the spectral model. Figures 15 and 16 show a comparison of radiometric model's results for TNT and ENE respectively against the BFII collections with the radiometric model represented by a solid red line and the data from the spectrometer by blue dots. The two events, 164DAT40, a 50kg

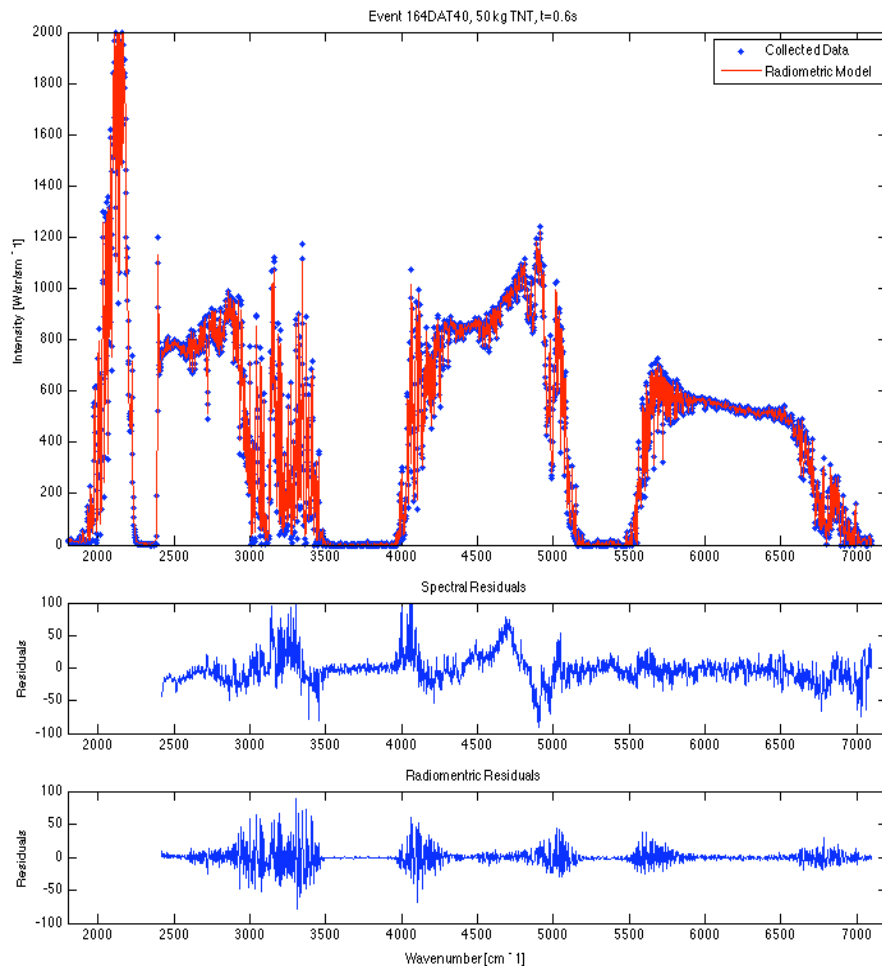


Figure 15. Panel 1 depicts a 50 kg TNT detonation from the BFII tests compared again the data collected by the MR-154 FTS spectrometer. The residuals from the model and actual data from both the radiometric and spectral model are provided in panel 2 and 3.

TNT detonation, and 164DAT43, a 50 kg ENE2 detonation seen in Figures 15 and 16 respectively provide a typical portrayal the data from this study. While a complete comparison of all the data is not provided,

the data sets presented provided a good representation of all the data. The residuals from collected data and the respective model are also seen in the lower panel in Figures 15 and 16.

The five-band radiometric model produced a spectrum that was comparable to the spectral model's results as seen in the residuals in Figures 15 and 16. Considering the radiometric model only uses five data points to produce the spectrum, where the spectral model used thousands of data points, the radiometric model performed exceptionally well. The residuals from spectral region below 2200cm^{-1} are

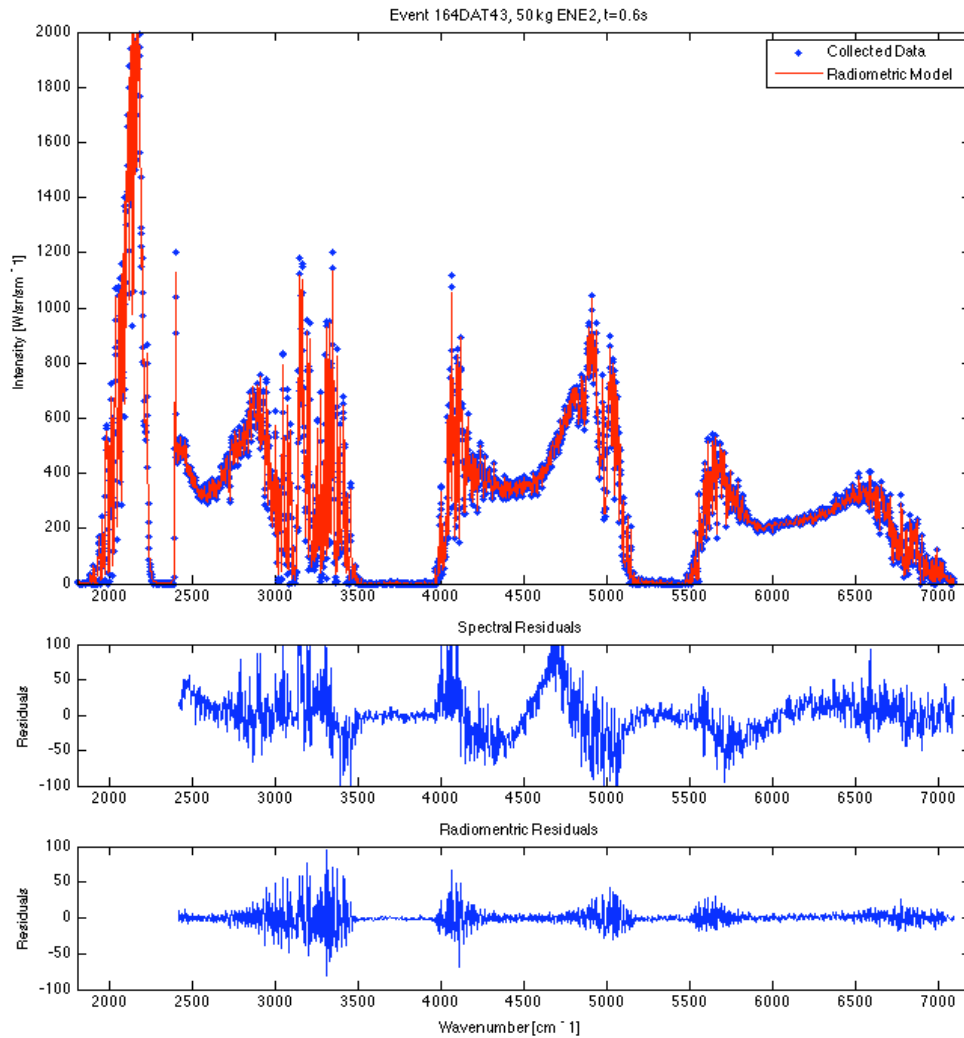


Figure 16. Panel 1 depicts a 50 kg ENE detonation from the BFII tests compared again the data collected by the MR-154 FTS spectrometer. The residuals from the model and actual data from both the radiometric and spectral model are provided in panel 2 and 3.

not displayed, as that region did not fit well in the original spectral model and the radiometric model also inherited these problems within this region. This region has been previously addressed as a deficiency of the model, partially due to the large simplifications made to produce this simplified phenomenological based model [1].

To quantify the differences between the spectral and radiometric model the Root Means Squared Error (RMSE) will be used which is seen in equation 9. The resulting residuals from the spectral and radiometric models fit to the apparent intensity collected from BFII will be examined within the approximate rang of 2200-7100cm⁻¹.

$$RMSE = \sqrt{\frac{\sum_{i=1}^n (I_{obs,i} - I_{mdl,i})^2}{n}} \quad (9)$$

For the TNT event, seen in Figure 15, the spectral model produced an RMSE = 25.7 W/sr/cm⁻¹ at t=0.6s, where the radiometric model produced an RMSE =15.0 W/sr/cm⁻¹ with respect to the BFII data. The ENE event, depicted in Figure 16, produced an RMSE = 34.1 W/sr/cm⁻¹ at t=0.6s for the spectral model, where the radiometric model produced an RMSE =13.3 W/sr/cm⁻¹ with respect to the BFII data. In general the ENE events had a higher correlation to the BFII data than the TNT events. Surprisingly the radiometric model produced a better with fewer data points than the spectral model did. While the spectrum was successfully modeled using only five data points from integrating over spectral bands yielding the total intensity, the actual fit parameters that drove the spectral model are now examined.

The five radiometric fit parameters, size, temperature, soot, H₂O and CO₂ concentrations from the TNT and ENE case will be directly compared to the spectral model's results from Gross's work [1]. These comparisons are seen in Figures 17 and 18 and are from the same test cases presented above. Both the TNT and ENE case show a high correlation between the derived temperatures slightly overestimate the initial temperature. The radiometric model initially computed the temperature 10-15% larger than that of the spectral model. This discrepancy is typically observed during the initial stage of the fireball's life where its emission properties are highly Plankian. This is because during the initial stages of the fireball,

the source is considered to be optically thick [1] masking the individual excited gas emissions and with the primary features being comprised of temperature and area.

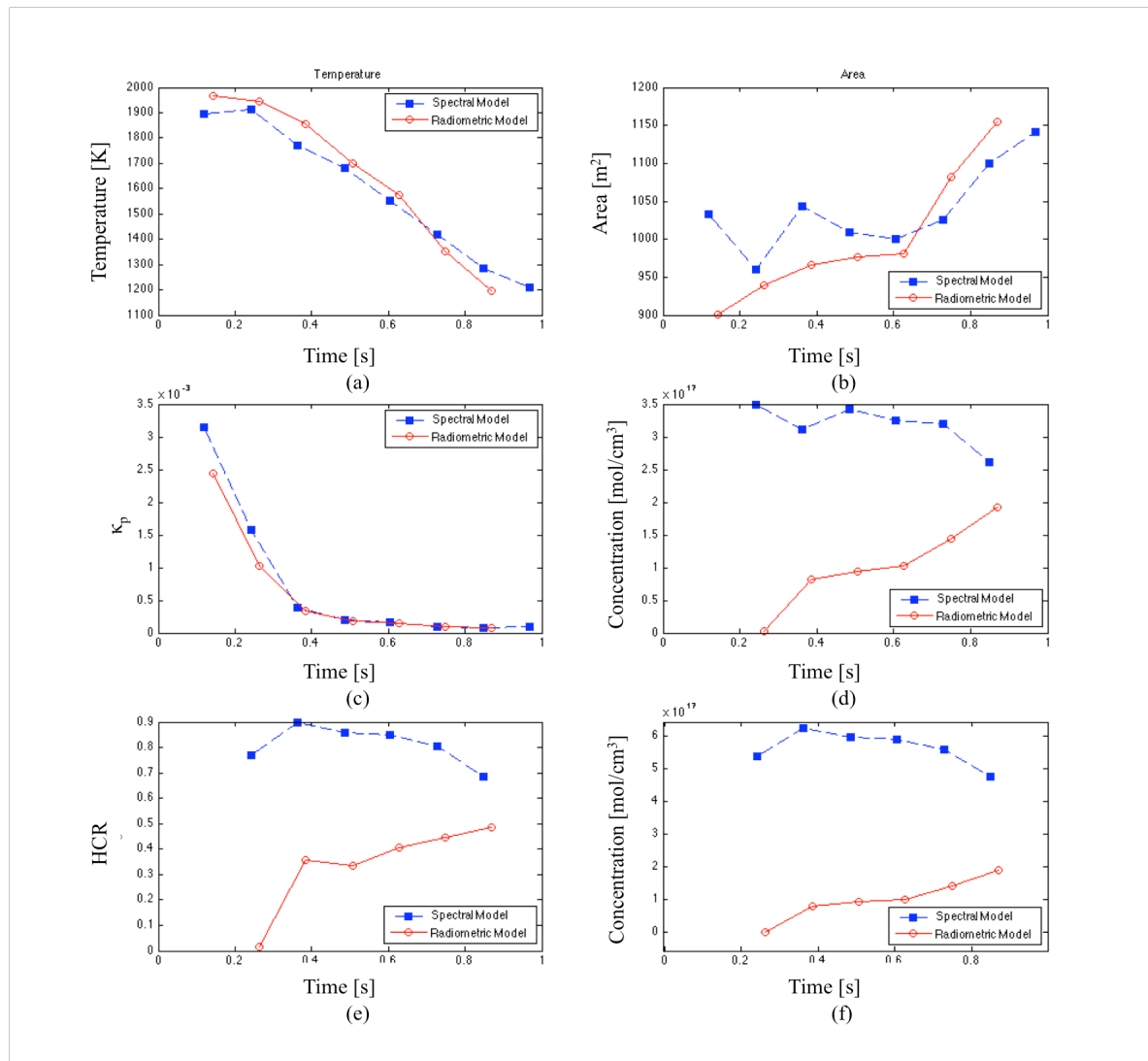


Figure 17. Feature comparison between radiometric and spectral model for event 164DAT40, 50kg TNT for (a) Temperature, (b) Area, (c) Soot Constant, (d) H₂O concentration, CO₂ concentration

The second feature, area, is typically estimated lower than the spectral model in the initial stages of the fireball. This could be related to the slight overestimation of temperatures that were also observed in the early stages of the fireball from the radiometric model. Another aspect of error within this area could be the assumption of the emissivity equaling one within band one, 2120-2280 cm⁻¹. This approximation

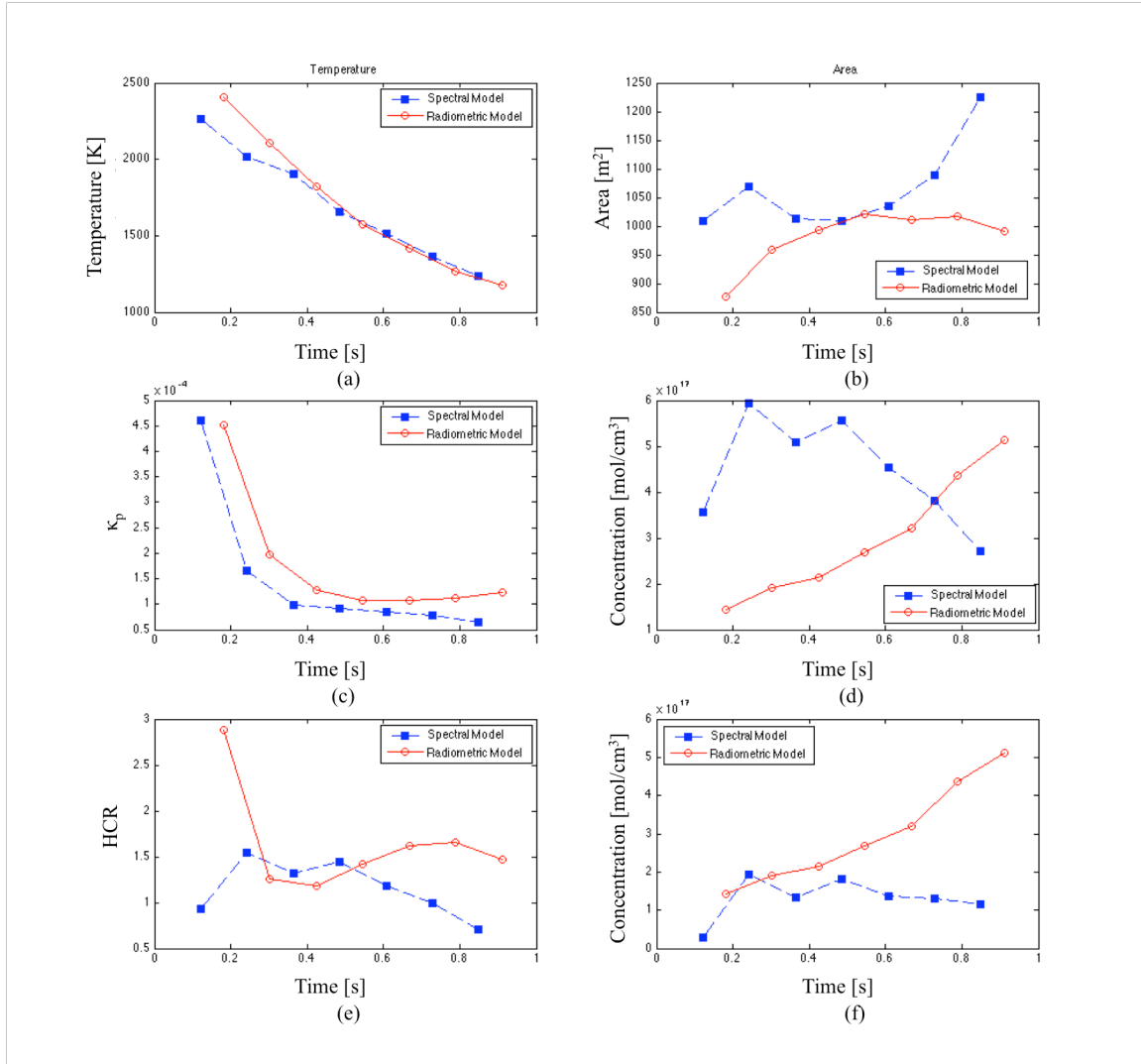


Figure 18. Feature comparison between radiometric and spectral model for event 164DAT43, 50kg ENE2 for (a) Temperature, (b) Area, (c) Soot Constant, (d) H₂O concentration, (e) HCR, and (f) CO₂ concentration

could be responsible some of the deviations observed in approximating the area of the fireball. Beyond the initial discrepancies observed between the spectral and radiometric model with regards to area, generally they agree deviating less than 12% from the spectral model's area fit parameter. The ENE case depicted in Figure 18 shows a slight problem with matching the area later in time but remains within a 24% of the spectral model's area fit parameter.

The third feature, soot concentration, is also depicted in Figure 17 and 18 and also shows a high level of correlation to the spectral models results. There is a slight trend of underestimating the initial concentration. This is not entirely unexpected as both the temperature and area had consistent fitting issues

in the first few data points compared and that each fit parameter is sequentially calculated carrying over errors present in the previous fit parameter. A likely explanation is that during these initial stages the fireball is highly Plankian and optically thick making any measurement of a selective emitter very difficult and possibly unreliable. These differences could be the result of spectrometer incorrectly calculating the correct intensity for the first scan, which was discussed in the appendix. This could easily be investigated by deploying a radiometer, in place of the spectrometers used in this study, to derive the fit parameters discussed above and provide beneficial findings to help identify these initial discrepancies observed. If the results from the radiometers do not show any discrepancies in the initial stage of the fireball for these three features, would indicate a large probability that the errors inherent in an estimation of intensity from an interferogram. Comparing these three fit parameters, temperature, area, and soot concentration fit the spectral model to within 24%.

The H₂O and CO₂ concentrations, along with the HCR derived from the radiometric model exhibited a deviation of upwards of 333% when compared to the parameters derived from the spectral model. In contrast to the highly correlated fit parameters previously discussed, the values derived from the radiometric model for H₂O and CO₂ concentrations did not trend well with the spectral models results. This may be due to the presence of errors from the previous fit parameters that inhibit the precision required to provide good trending of these variables. When the relative concentrations were interpreted into a HCR, the expected separation between the TNT and ENE events remained relatively intact as seen in Figure 19. Maintaining this separation between TNT and ENE when examining the HCR is important because the previous spectral model demonstrated a clear characterization ability utilizing the HCR achieving a FR of over 17.5 [1]. While the calculated HCR for both TNT and ENE are lower than known chemical composition of the explosives, they maintain their respective ratio of approximately 5-1 between the ENE-TNT events. The FR calculated from the radiometric HCR was 12.9, which provides a reduced classification capability. Table 5 lists the relative stoichiometry for the events observed in BFII [1].

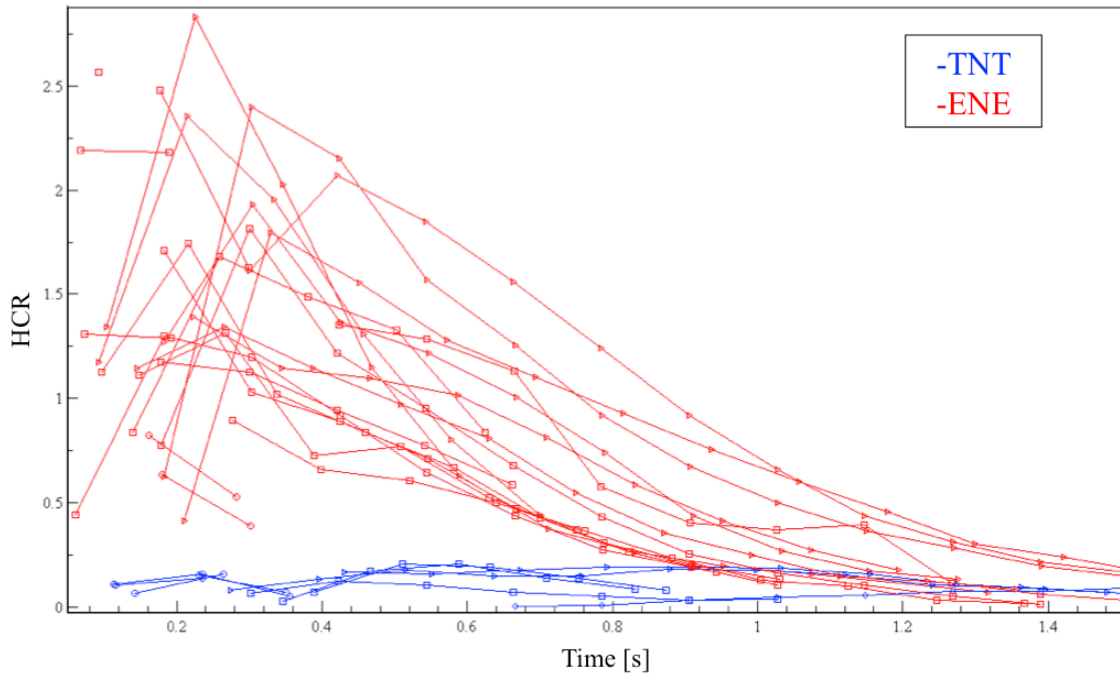


Figure 19. The HCR for all the ENE and TNT events showing the relative separation between the two classes

Table 5. The relative stoichiometry for each HE type used in BFII [1]

HE Type	Stoichiometry
TNT	0.79
ENE0B	21.3
ENE1	6.7
ENE2A	5.8
ENE2B	6.7

Continuing the investigation for the five-band radiometric model’s classification potential the FLD was applied to the derived fit parameters. The five fit parameters that yielded the highest separation capability from applying FLD, occurred with the first initial detection points. The FLD produced that largest FRs which indicated that the initial stages of the fireball had the highest classification potential. Figure 20 shows each event projected onto a fisher line, or x-axis, where Class 1 is comprised of the TNT events and Class 2 encompasses the ENEs and yielding a FR of 24.9. Using the FLD with the raw integrated intensities provided a direct comparison classification potential against the fit parameters they derived. The raw integrated intensities resulted in a reduced FR of 4.2. This indicates that the integrated

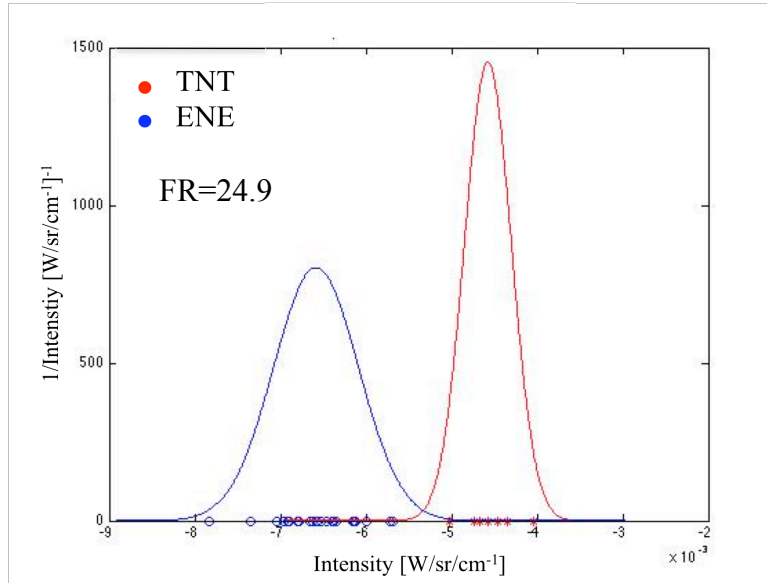


Figure 20. Data projected on the fisher line with a Gaussian representation of the data projection.

intensities used to calculate the fit parameters do not provide a good classification potential when they are not interpreted into fit parameters. By interpreting the raw intensities into the fit parameters discussed above increases the FR by a factor of five.

Using the FLD to produce a FR as a measure of classification capability, different times or stages within the life of the fireball were compared. The largest FR calculated typically occurred at the beginning of the collection and was diminished in a linear fashion as time progressed forward. The projection vector from the FLD indicated that the soot concentration had the largest magnitude, which dominated the other projections by more than a factor of ten. Due to this sizeable contribution from the soot concentration, the projection vectors with the smallest magnitude were left out one by one, repeating the FLD each time. This was to investigate and identify which fit parameters and combination of features provided the largest role for discrimination. A combination of three parameters, which included temperature, soot concentration and HCR, yielded a similar FR of 24.1. This was not entirely unexpected, as these three fit parameters require five bands to be calculated which did not provide a large insight to further feature or band reduction methods. While reducing the number of bands or fit parameters required to create the spectral model is beyond the scope of this work, the findings of this study do not rule out the possibility. Overall the concept of using a combination of passive radiometers in place of a full collected spectrum for the purpose of

discrimination was proven. To accomplish this several restraints has to be placed on band selection to ensure the derived intensities could be properly mapped to the required fit parameters. Given the fact that the radiometric model uses several orders of magnitude fewer data points than the spectral model does, the correlation is considered to be quite good. These characterizations are achieved using a five-banded radiometric model with the presence of a large amount of prior knowledge concerning the explosive types. While TNT and ENE were separated from each other, the introduction of a third and unknown class may not be able to be separated. Currently the utility of this model is largely based upon data sets that are well understood.

4.2 Revised Radiometric Model

Building upon the radiometric model's successes and problems encountered, led to a revised radiometric model. This section will discuss the modifications that were made from the original five-band radiometric model discussed above. This will be followed an examination of the results of these changes using on TNT and ENE event from BFII. Two primary changes were made to the original radiometric model. First the assumption of the emissivity being equal to one in band 1 was removed. This required five new bands sizes and widths to derive the five fit parameters. To calculate the color temperature two bands were used as before. Applying the same methodology above, two bands were placed at 4350-4530 cm^{-1} and 6000-6200 cm^{-1} . The area, soot, H_2O and CO_2 concentration were found by placing bands at 3850-4350 cm^{-1} , 3200-3600 cm^{-1} and 4700-5800 cm^{-1} . These three bands had different optical thicknesses that traveled through the same path. This allowed for these remaining variables, area, soot, H_2O and CO_2 concentration, to be derived from these band combinations. The second change was how the model was fit to the data. Previously each parameter was sequentially fit which potentially carried over and increased the error present from each previously calculated fit parameter. To correct for this each fit parameter was matched to the data concurrently with the exclusion of the color temperature calculation. As with the original radiometric model, color temperature is still calculated first before any of the other fit parameters. Calculating the color temperature is a proven and a process that is generally of high confidence providing the remaining fit parameters a reliable estimation to begin with. Two data sets were used for to test this process were the same two test cases presented in the original model above. These data sets were a 50kg

TNT, 164DAT40, and a 50kg ENE2, 164DAT43. The TNT test case produced a maximum residual of 27 W/Sr/cm⁻¹ from the revised radiometric model where the spectral model produced 40 W/Sr/cm⁻¹ as seen in Figure 21 and 22 respectively. For the ENE test case, the radiometric model produced a maximum residual

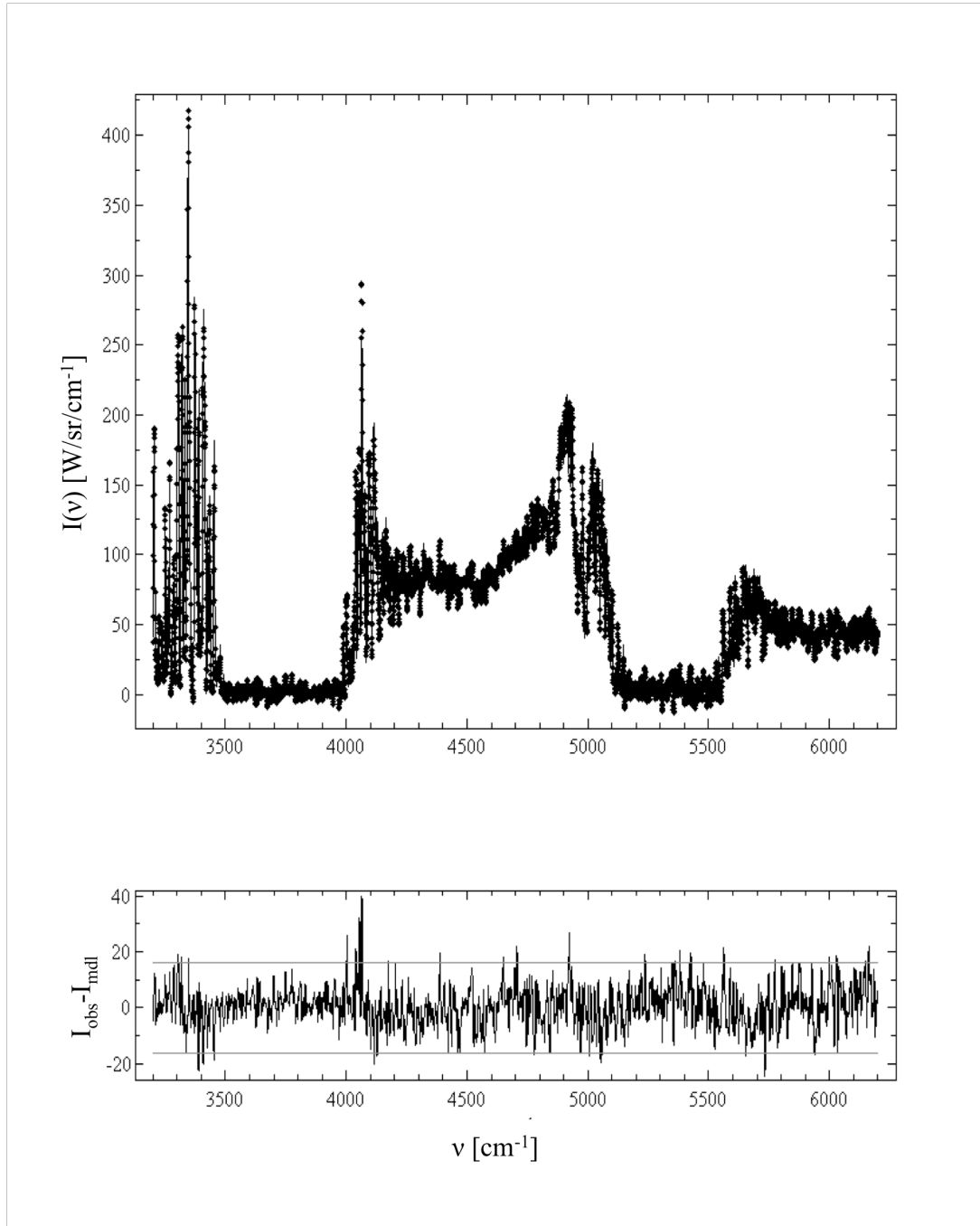


Figure 21. Top to bottom panel: Spectral model fit to the FBII data followed by the residuals present from comparing the spectral model to the BFII data.

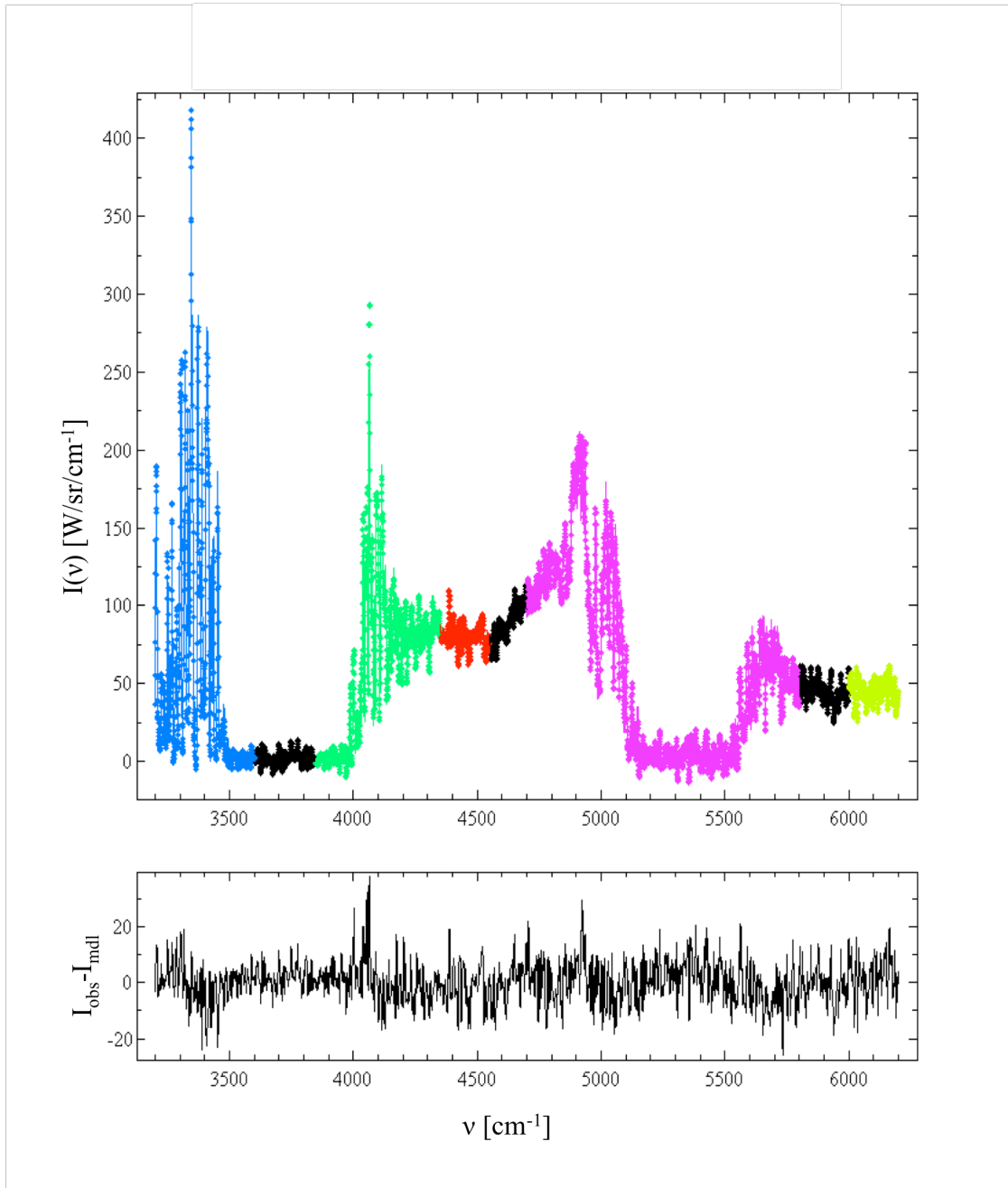


Figure 22. Top to bottom panel: Radiometric model fit to the FBII data with the band selected shown in color followed by the residuals present from comparing the spectral model to the BFII data.

of 59 W/Sr/cm^{-1} where the spectral model produced 41 W/Sr/cm^{-1} as seen in figure 23 and 24 respectively. Overall the maximum residuals were present were reduced by a factor of approximately two in both cases. Overall the TNT had lower residuals than the ENE case, which is a similar result of from the original model.

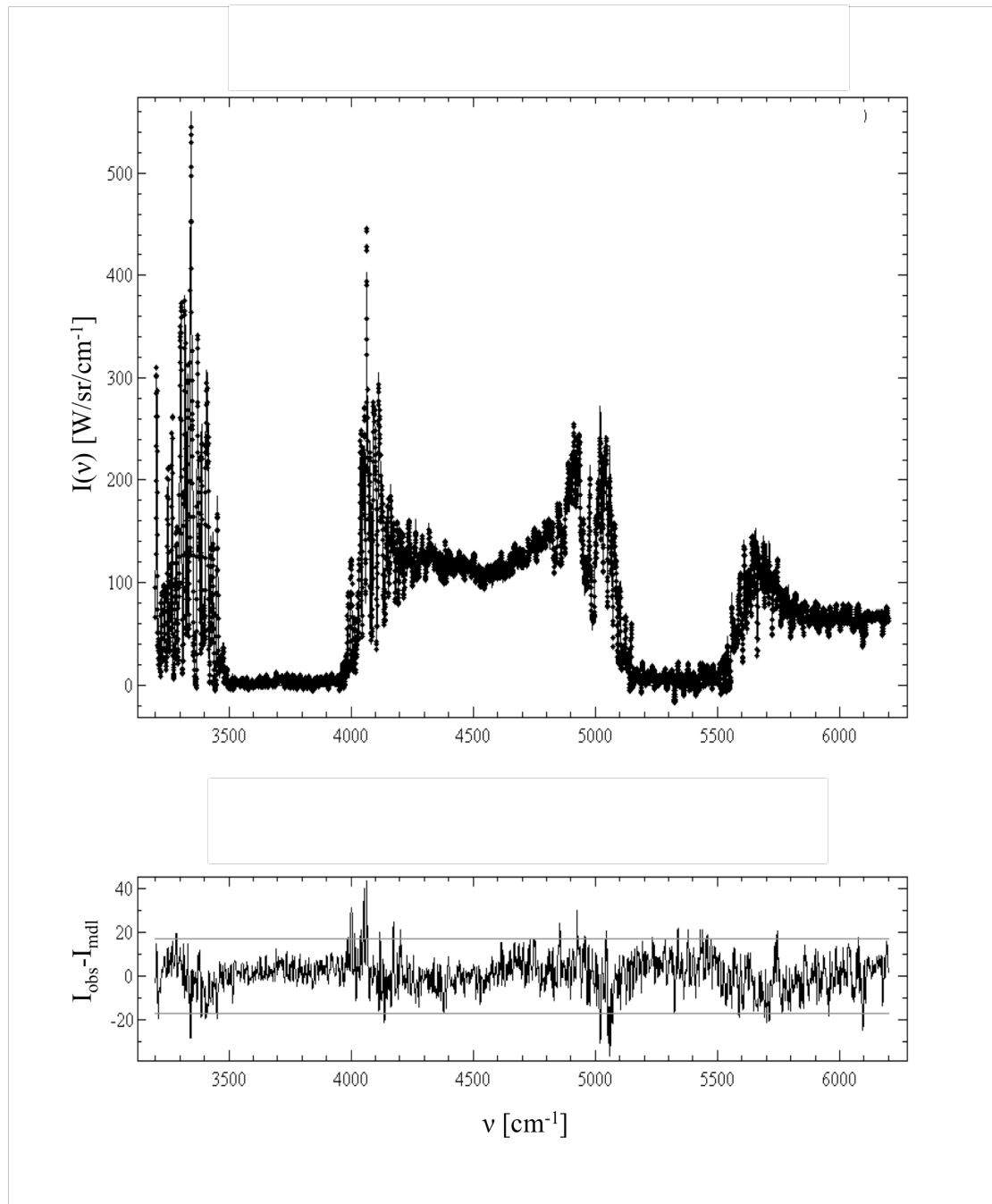


Figure 23. Top to bottom panel: Spectral model fit to the FBII data followed by the residuals present from comparing the spectral model to the BFII data.

Color temperature was calculated first with the remaining four fit parameters being concurrently calculated. This provided an estimation of temperature, area and soot concentrations to with a maximum error of 9.9% at $t=0.6s$ to the spectral results. The H_2O and CO_2 concentrations to were computed to have

no than a 17% deviation at $t=0.6s$ from the spectral fit parameters. A comparison of the radiometric and spectral results for each feature for TNT test case is seen in Figure 25 and the ENE test case is depicted in Figure 26. The HCR that resulted from the revised radiometric model produced much improved it to the

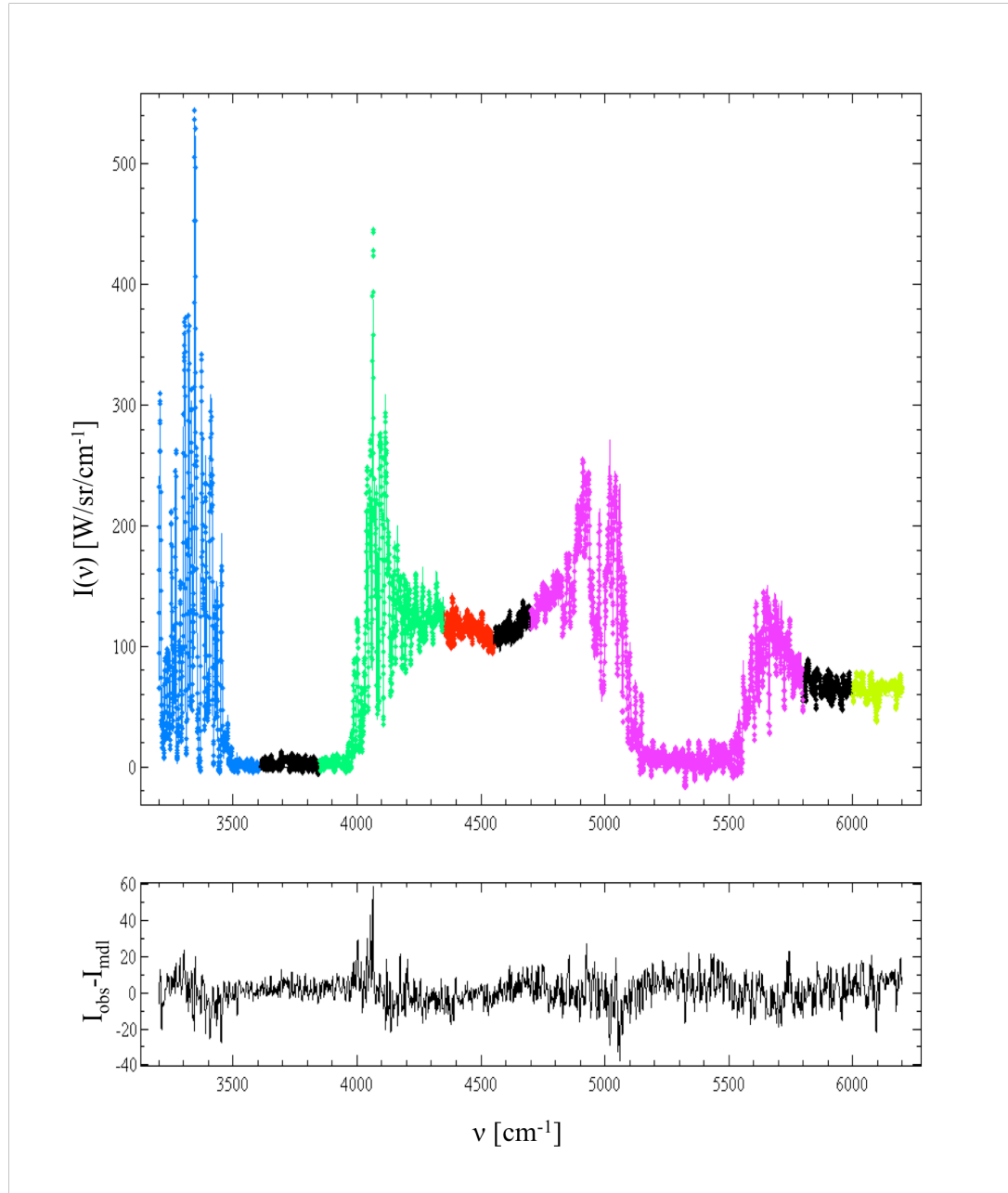
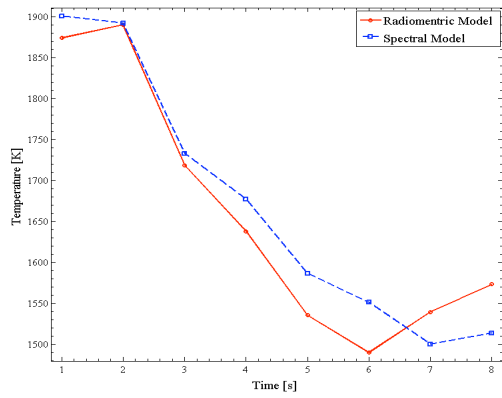
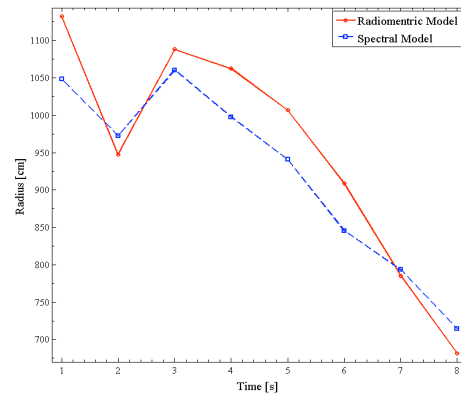


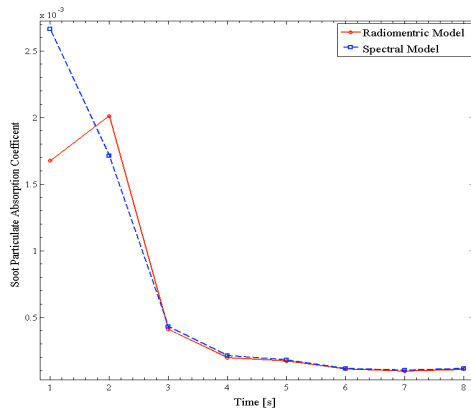
Figure 24. Top to bottom panel: Radiometric model fit to the FBII data with the band selected shown in color followed by the residuals present from comparing the spectral model to the BFII data.



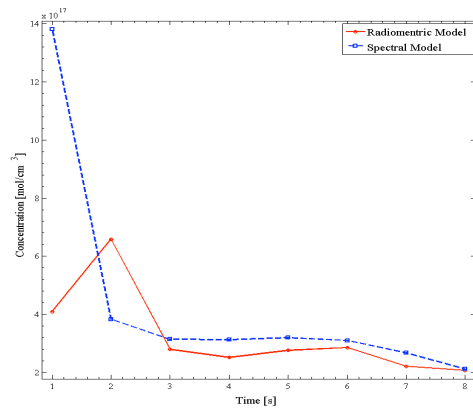
(a)



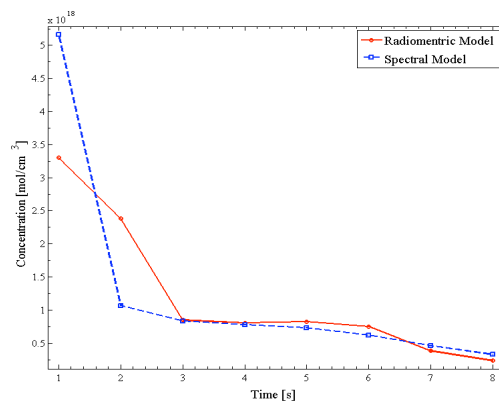
(b)



(c)



(d)



(e)

Figure 25. Comparison of the five fit parameters for a 50 kg TNT, event 164DAT40, depicted in blue dashed lines from the revised radiometric model compared to the spectral model shown by a solid red line for (a) temperature, (b) size, (c) soot concentration, (d) H₂O concentration and (e) CO₂ concentrations

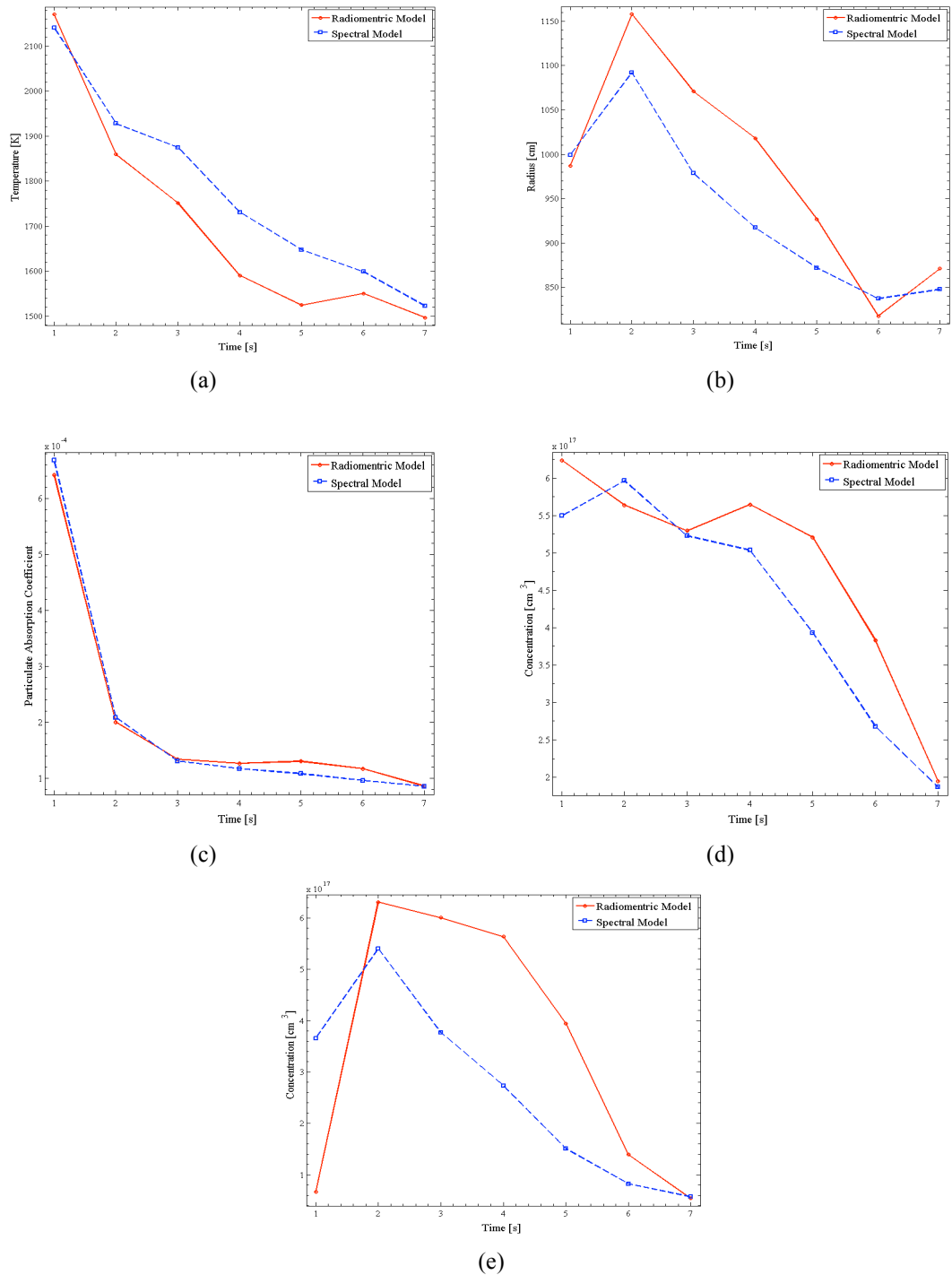


Figure 26. Comparison of the five fit parameters for a 50 kg ENE2, event164DAT43, depicted in blue dashed lines from the revised radiometric model compared to the spectral model shown by a solid red line for (a) temperature, (b) size, (c) soot particulate absorption coefficient, (d) H₂O concentration and (e) CO₂ concentrations

spectral model's HCR. The ENE case did overestimate the first point in the HCR, which is not entirely unexpected. The initial fit parameters points for H₂O and CO₂ were expected to be somewhat inaccurate due to the initial optical thickness of the fireball during these times. Ignoring these initial points produced a good approximation with a maximum deviation of 100%. A comparison between the revised radiometric model and the spectral model are seen in Figure 27. These improvements to the model only examined two data sets. While these two test cases used were representative of the data in with the original radiometric model, this may not be the same case with the revised radiometric model. Examining the entire data set would provide a more robust set of results from the revised radiometric model.

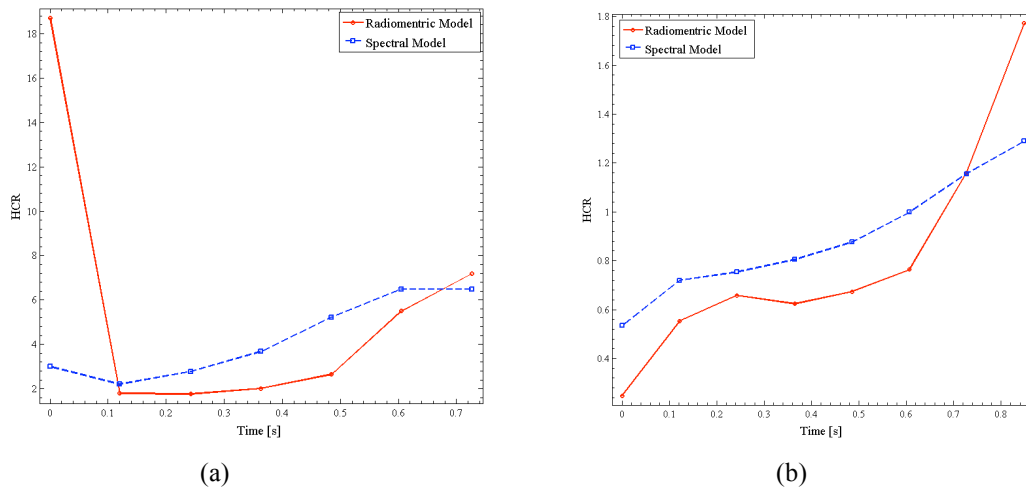


Figure 27. HCR for the revised radiometric model represented by solid red line and the spectral model represented by a dashed blue line for the (a) ENE and (b) TNT test cases.

The revised radiometric model improves upon several of the problems encountered with the original radiometric model. The fitting to the model is improved and all five fit parameters were derived with a higher degree of agreement with the spectral model's fit parameters. The HCR from the revised radiometric model produces values that closely match those of the relative stoichiometry of TNT and ENE. The initial findings from the revised radiometric model show promising results to perform classification using five radiometric bands to perform classifications. Moving past interpreting radiometric intensities into fit parameters, the second method that linearly interpreting the raw intensities to perform classification is now examined.

4.3 Radiometric Band Search Results

A search performed over the MWIR spectrum, 1800-6200cm⁻¹, was completed using a combination of two, three, and four radiometric bands. Using a minimum amount of optimization, the code was able to calculate the FR from a single cause using two bands within 0.12s. Considering the large amount of band combinations possible, symmetry was implemented to exclude redundant calculations that contained the same bands in an effort to reduce the overall calculation time. A five-band search was excluded due to the time computational times required to perform each search routine with is seen in Table 6. The times listed in Table 6 are based upon multiplying the individual calculation time stated above by the number of calculations required to compare all unique band combinations. This systematic approach selected every combination using the criteria previously stated in chapter 3. The top results from applying FLD and calculating the resulting FR are seen in Table 7. As expected the FR increased with each additional band used in the FLD pattern recognition tool. Throughout this study several data sets were removed during the five-band radiometric model investigation. Because of this the, two primary data sets were examined in an attempt to match the work performed for the five-band radiometric model. The first set includes all the data and the second only includes the data sets that were able to produce fit parameters within the defined bounds. As the data sets were reduced, the FR increased across the board. Because HE fireballs can inherently have a large variation between similar events all of the data sets were included as much as possible within this examination.

Table 6. Computational times required to complete each search routine for the 2, 3, 4 and 5 band combinations.

	2 Band	3 Band	4 Band	5 Band
Time required	12 minutes	4 hours	17 days	+4 months

Table 7. Max fisher ratio achieved from the multiband search using two data sets; one including all data observations from BFII and the seconds only containing the data sets that were able to produce fit parameters for the five-band radiometric model.

Data Set	2 Band max FR	3 Band max FR	4 Band Max FR
All Data	6	15	22
Data sets that derived fit parameters	12	22	NA

Two Bands.

The two-band search produced three primary areas within the spectrum that showed potential for discrimination. The three regions were centered around 2600, 4600 and 6100 cm^{-1} . Originally it was hypothesized by the author, that the best discrimination would result from similar bands used to drive the five-band radiometric model, but this was not the case. This hypothesis was based upon believing the a band selection around the previously defined regions to extract these feature would provide the best results. The two-band combination that yielded the highest FR was calculated from two bands that were in close proximity to each other. This closely contained combination of bands produced a FR double of that of other regions. This observation will be typically referred to as a FR spike. The top result had a FR of 6.2 using a center bandwidth of 2650 and 2850 cm^{-1} . Spectrally this occurred in a region with known for very small amounts of HCl and no CO or CO₂ emissions present. A small amount of H₂O emission also occurs within this region and can be seen in Figure 28, which shows the relative molecular emissions, transmittance of

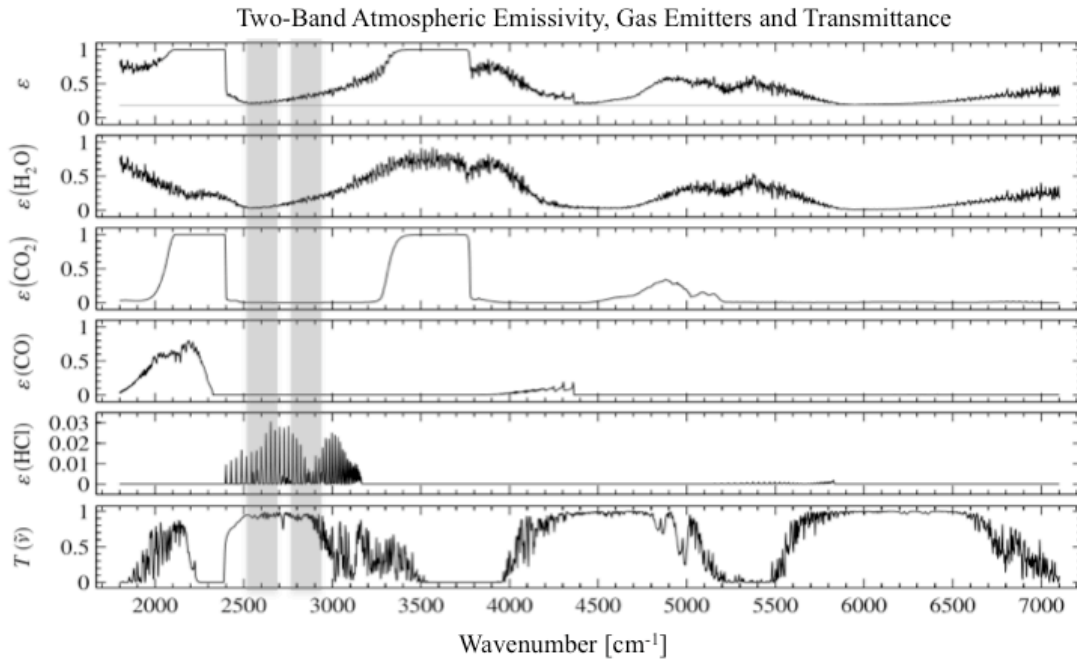


Figure 28. Top to bottom panel: Spectral emissivity of the fire ball in black and the soot emission in gray; spectral emissivity of H₂O; the spectral emissivity of CO₂; spectral emissivity of CO; spectral emissivity HCl; spectral transmission of the atmosphere; grey regions representing the two best bands from the two-band search that produced a FR of 6.2.

the atmosphere and highlights the placement of the best band combination from the two-band search. Considering the small gas emissions present in this region it is likely the soot the largest contributor to the intensity with respect to the hot gases. The results from the two-band search results are seen in Figure 29, which shows each band color-coded and connected the combination the produces the respective FR. An unexpected trend observed where the amount of band combinations that were very close or overlapping with each other seemed to produce the largest FRs.

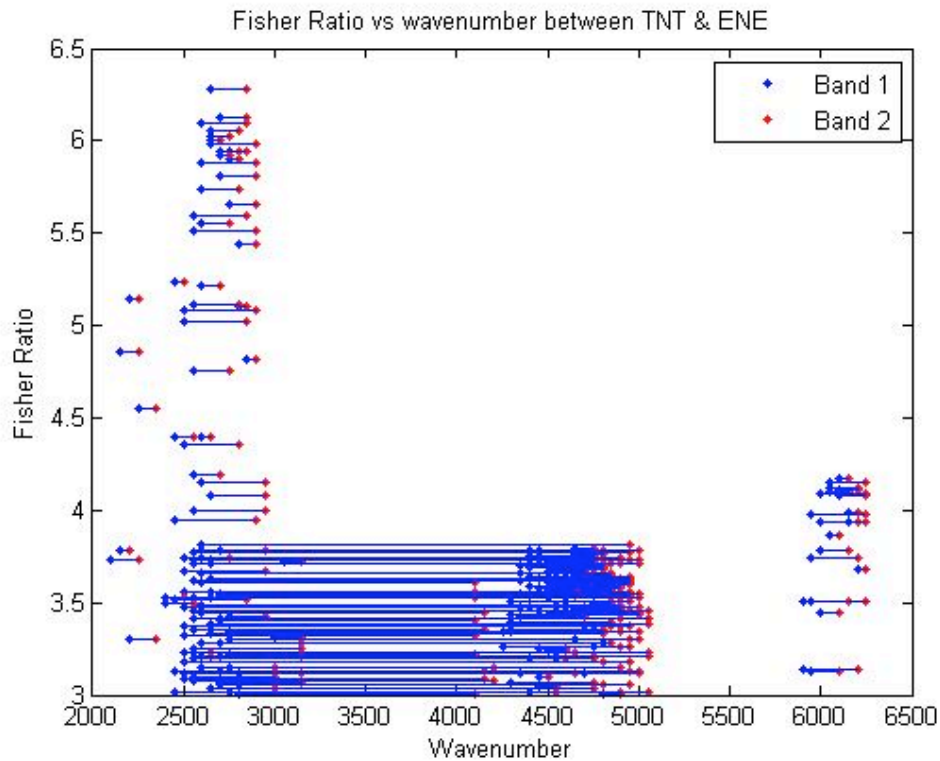


Figure 29. Band combinations that produced a FR greater than 3 with band 1 represented by a blue dot and band two by a red dot. The blue line connects the two bands that produced the respective FR.

By reducing the data to only include the data sets that produced reasonable fit parameters greatly increased the calculated FR. The data sets that were excluded may have had a low signal to noise ratio (SNR) that prevented them from correctly calculating the a reasonable fit parameter discussed in the previous section. As seen in Figure 30a & 30b the maximum fisher ratio is double that of the original search that

included all of the data sets. By removing the noisy collections and only using data sets known to have a good SNR the classes had a larger separation when the FLD was applied. This difference in separation capability observed between the two data sets seen in Figure 31 a & b which shows the classes projected on the best fisher line with their probability densities function (PDF) overlaid on top of them.

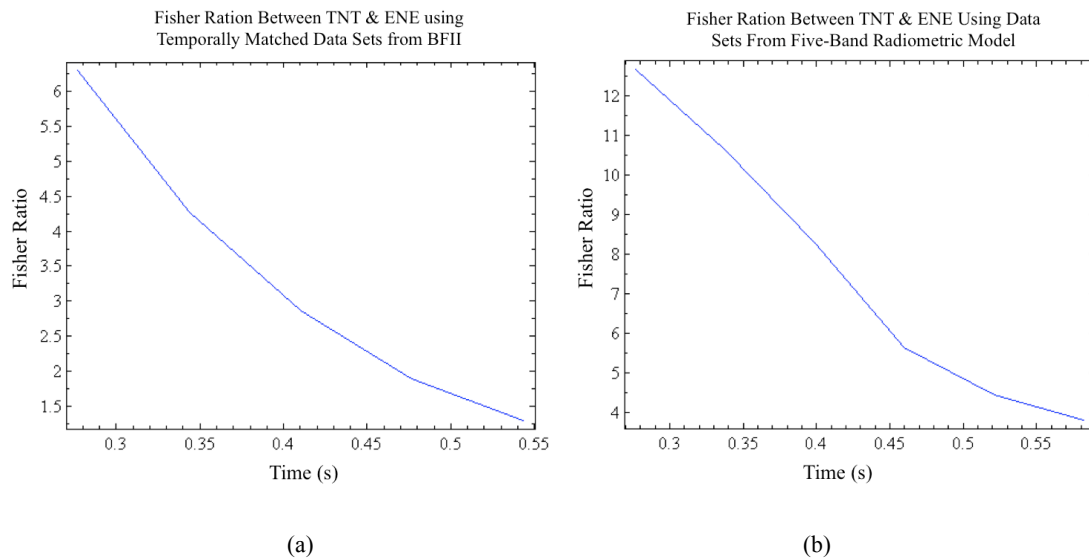


Figure 30. Best Fisher Ratio achieved with respect to time for (a) all data sets from BFII and (b) only the data sets that produced fit parameters from the five-band radiometric model.

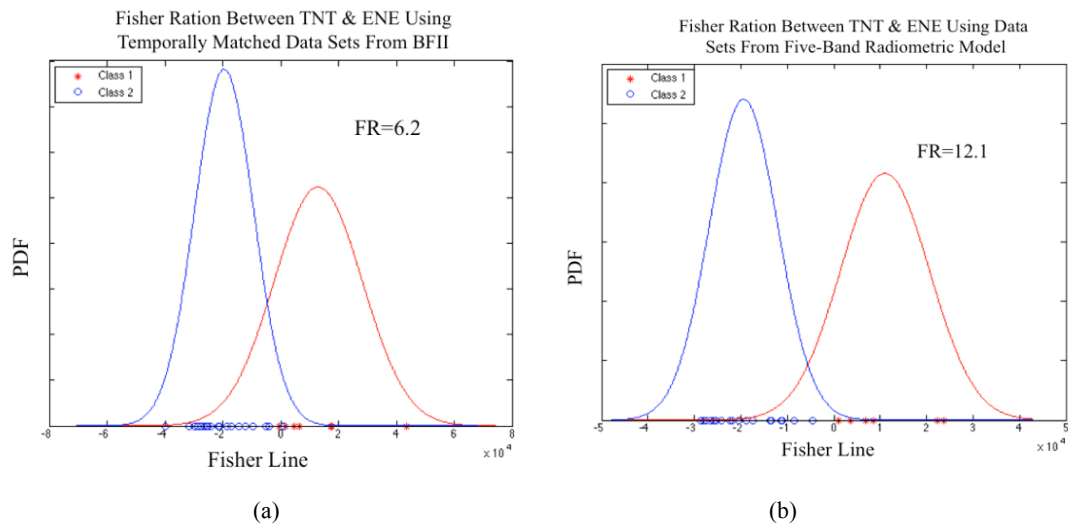


Figure 31. Class 1 and 2 projected onto the Fisher line with their respective PDF for (a) all data sets from BFII and (b) only the data sets that produced fit parameters from the five-band radiometric model.

Three-Band.

The three band searches results are displayed in Figure 32, which clusters the results of each band on top of each other in order to identify the regions that contribute to calculating a larger fisher ratio. The relative transmission and emissivity of known emitters in the atmosphere are also displayed in Figure 32. A FR spike is observed in the region near 5000cm^{-1} , and as stated before was not predominant in the two-band search but was present in the four-band search.

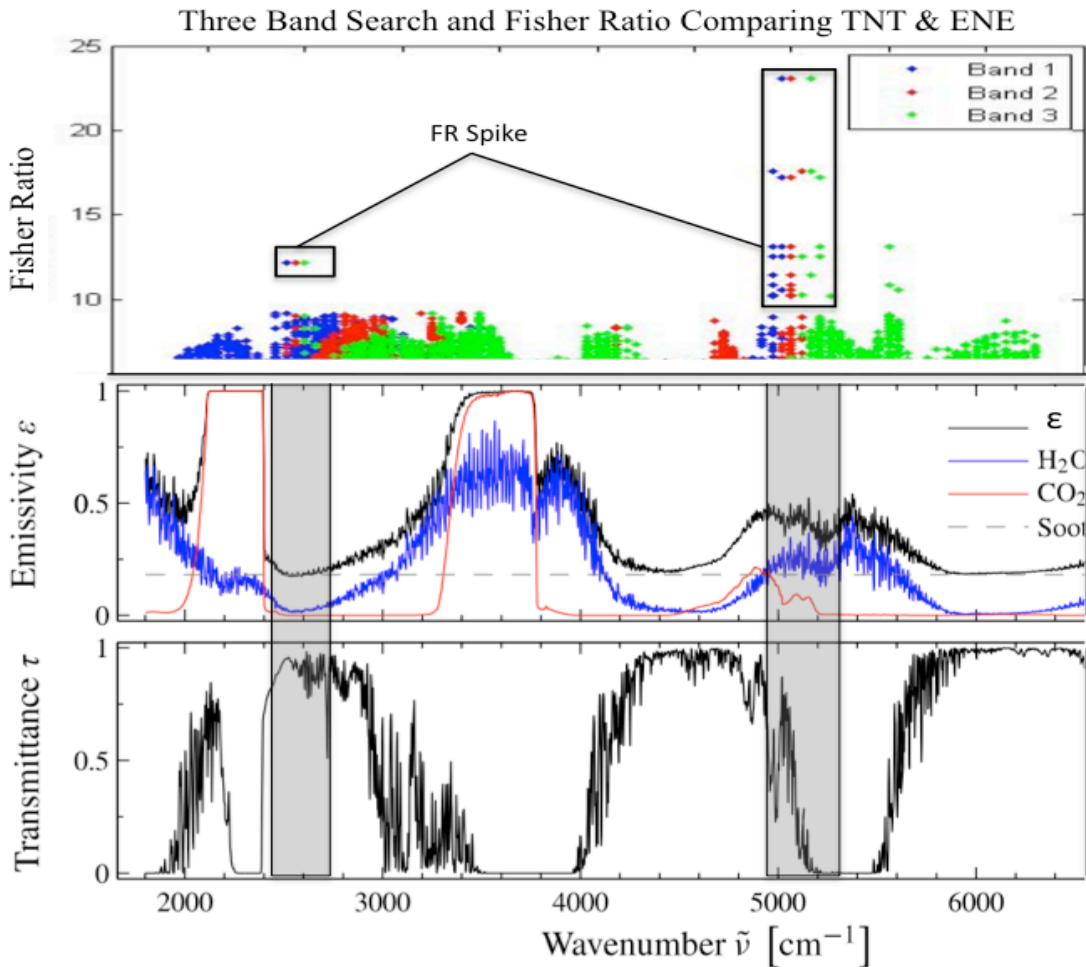


Figure 32. Top panel to bottom panel: FRs greater than 6 from the three-band search with band 1 represented in blue, band 2 represented in red and band 3 represented in green. The regions that produced high FR values are labeled as FR Spikes; The spectral emissivity of the fireball in black, H_2O in blue, CO_2 in red, and the soot represented by a dashed grey line; The spectral transmittance of the atmosphere. The semi-transparent grey regions represent the areas where the FR spikes resided.

This raises several questions to a validity of this region and if it was an artifact from the data set or a very precise discriminating feature. While these three bands do occur on a rapidly changing transmission

function the amount of overlap makes it hard to believe this could be the optimal selection for discrimination. The spectral emitters present within the FR spike bandwidth are seen in Figure 33. This clearly shows that CO₂ and H₂O are both present within this region. Also it's seen that the bands fall on to a rapidly changing area of the atmospheric transmission right next to a large absorption band, which is also seen in Figure 33.

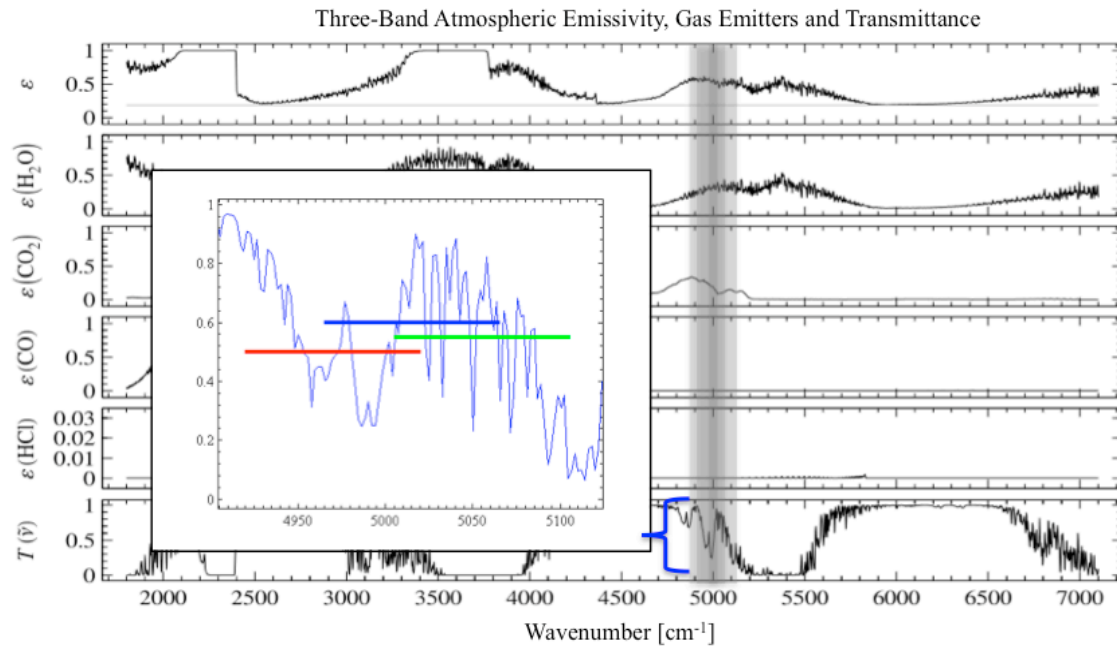


Figure 33. Top to bottom panel: Spectral emissivity of the fire ball in black and the soot emission in gray; spectral emissivity of H₂O; the spectral emissivity of CO₂; spectral emissivity of CO; spectral emissivity HCl; spectral transmission of the atmosphere; Grey regions representing the three best bands from the three-band search with a zoomed in region showing the band placement overlaid on the respective atmospheric transmittance.

To investigate the stability of this result, two tests were performed in this region. First the search was repeated limiting the search area just beyond these top bands and refining the step size. If the feature was real it was expected that a gradual rise in the FR would be observed as the search approached identified bands. The step size was reduced to 5cm⁻¹ and the results can be seen in Figure 34. Not only was a gradual rise observed as the bands from the three-band FR spike, but the FR also dramatically increased.

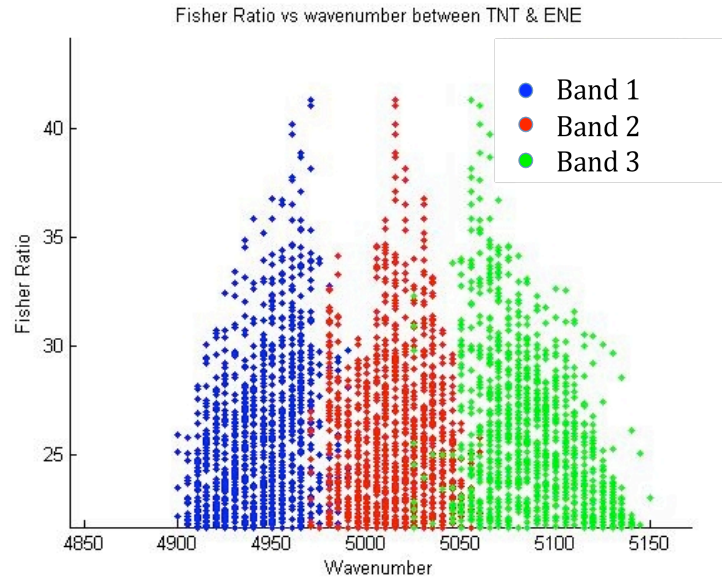


Figure 34. The center bandwidth placement from a refined three band search which reduced the band step size to 5cm^{-1} to identify more precise placement of band to achieve the best FR within the FR spike region. Band 1, 2, and 3 being labeled blue, red and green respectively.

The original FR of 22 rose to a value of 41.3 and resulted in a refined center bandwidth of 4970cm^{-1} , 5015cm^{-1} , and 5055cm^{-1} . The second test employed was to systematically leave one data set out (LOO) to try and identify a possible collection that was corrupting the results. This was done by using the previously identified top three bands and applying FLD while rotating one data collection out each time. The resulted from this are displayed in Table 7 and it was unable to locate a primary data set responsible for these results. With a $\text{FR}=41.3$ an obvious distinction within the intensities was expected to be observed. The integrated intensities for these regions were plotted which showed that each band was highly correlated with each other. As seen in Figures 35 and 36, the intensities from all three bands appear to be indistinguishable from each other. The three bands used were correlated with each other to by over 90%. The code used to calculate these results was also tested multiple times with known solutions and proved to be reliable. The spectrum from the FR spike bands is overlaid, as seen in Figure 37, which also shows that they spectral signature is also appear to highly correlated showing no noticeable difference that would allow for such a high discrimination.

To investigate the differences between the three best bands identified within the FR spike, the projection vector 'W' that produced a FR=41 at t=0.4s was saved. Using this W vector the intensity component projected from each band was summed with the other two bands on the fisher line over time.

Table 8. Results from the leave one out test examining three-band FR spike from observed

Data Set Removed	Fisher Ratio	Data Set Removed	Fisher Ratio
0	37.2922	30	48.5
4	36.7	31	33.5
5	36.1	32	35.8
7	39.7	33	37.7
8	37.5	34	37.3
17	36.7	35	36.5
18	35.6	36	38.8
19	36.4	37	37.2
20	35.5	38	34.8
21	37.1	39	37.2
22	40.2	40	37.3
23	37.5	41	37.4
24	43.3	42	38.4
25	40.1	43	37.3
28	34.6	44	37.3
29	35.4		

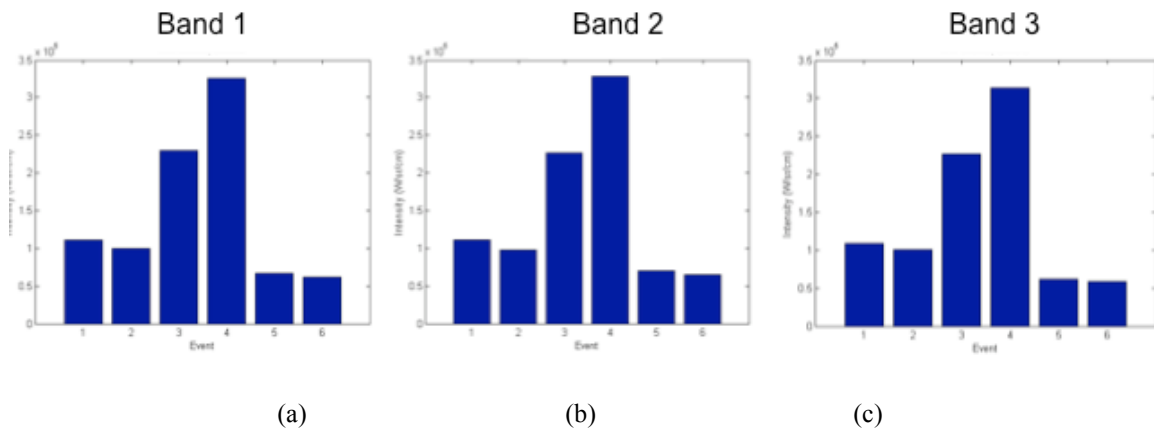


Figure 35. TNT intensities for each event within the three-band FR spike for (a) band 1,(b) band 2, (c) band 3. All three bands are highly correlated with each other.

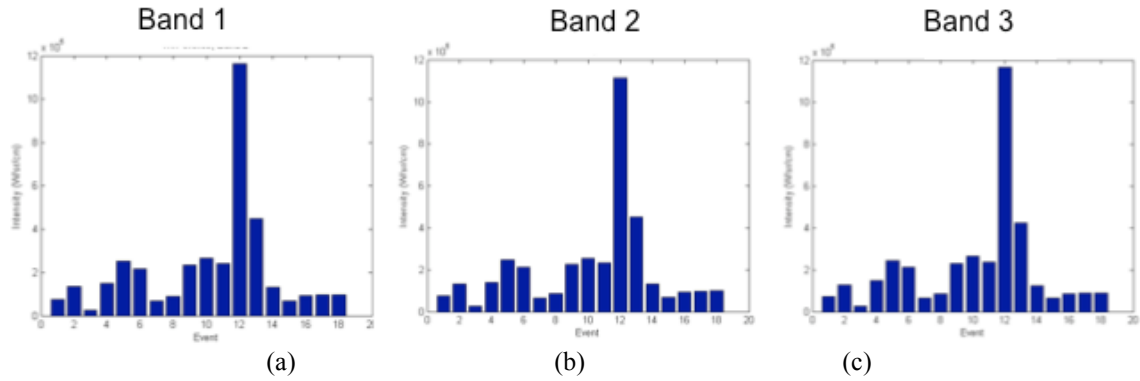


Figure 36. ENE2 intensities for each event within the three-band FR spike for (a) band 1,(b) band 2, (c) band 3. All three bands are highly correlated with each other.

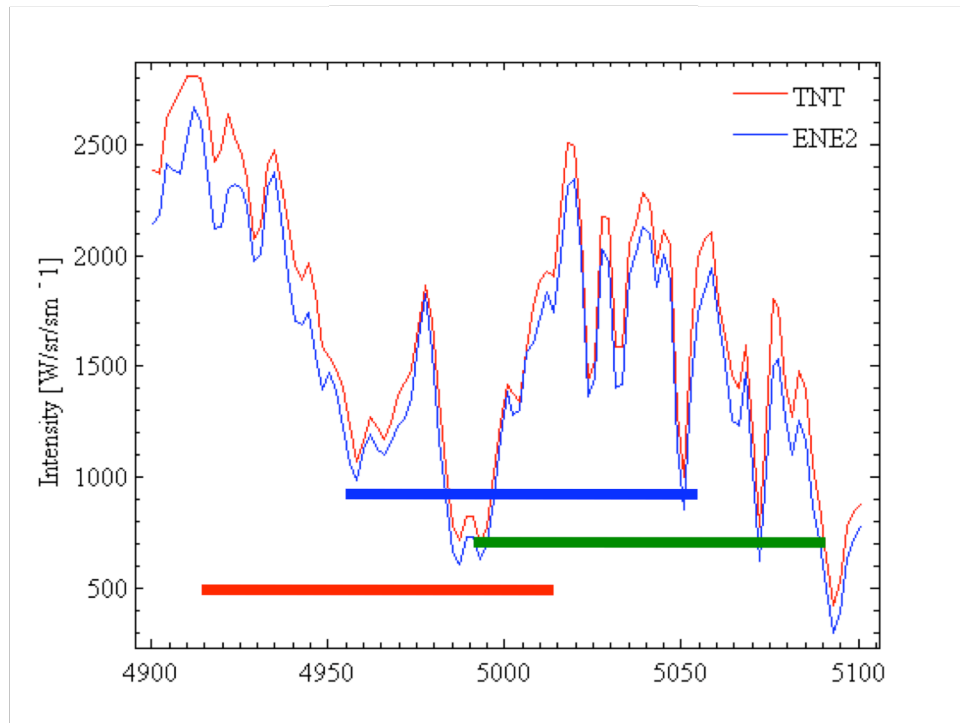


Figure 37. The TNT and ENE test case spectral signature overlaid on each other at $t=0.4s$ with the red line representing band 1, blue line representing band 2, and the green line representing band 3.

This shows how each event changes its position onto the fisher line over time using the same W projection vector. As expected, Figure 38 shows the TNT and ENE events achieve a maximum separation at $t=0.4$.

The events the do not trend with the majority of the data represent the 1000 kg detonations. Figure 39

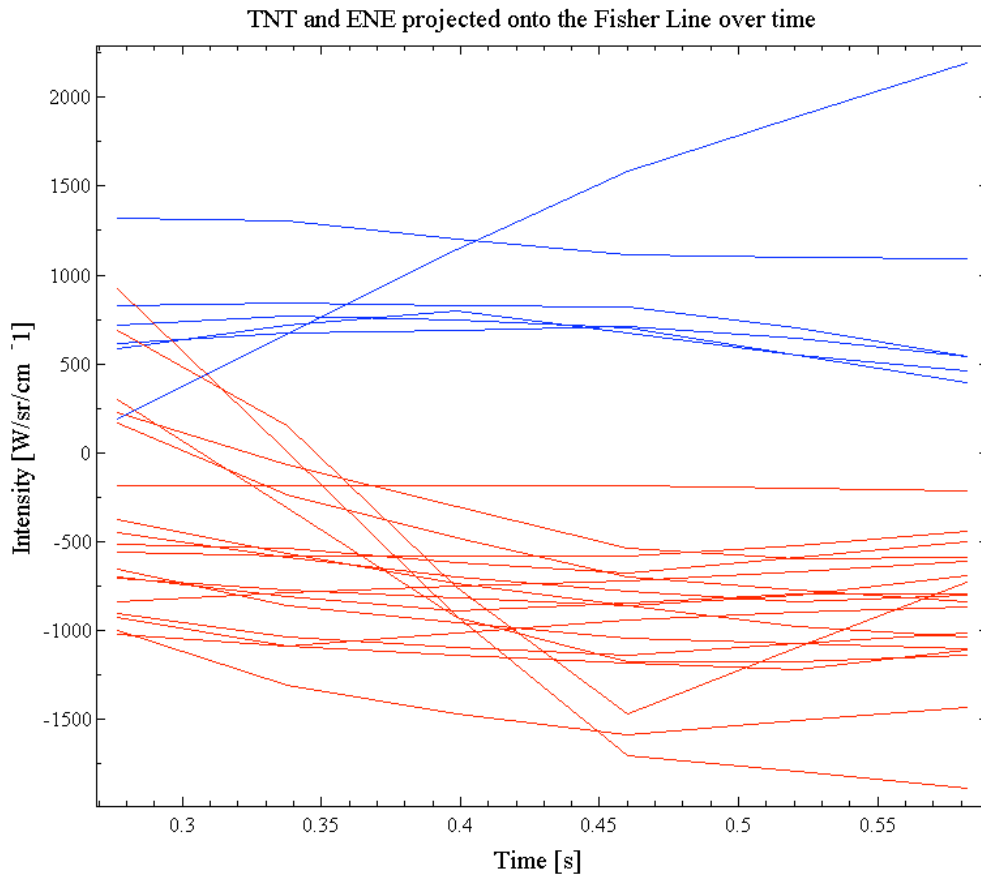


Figure 38. Intensities from each bands are summed on the fisher line over time using the projection vector that achieved a FR=41.

depicts the FR over time using the optimal FR spike bands that resulted in a peak FR of over 41. The time span uses the same range defined earlier that maximizes the overlapping data sets. Figure 39 shows that the maximum discrimination occurs later in the detonation as opposed to the previous findings indicated that maximum discrimination occurred at the beginning of detection which agrees with Figure 38. To further investigate the cause to the large classification potential within this region the orthonormal components from each band were examined using the Gram-Schmidt process. If there was a large difference between the bands this process should identify the vector components that are very different from each other that provide the exceptionally large FRs. To accomplish this, the vector components normal to each band are identified by calculating the projection of the perpendicular element with respect to the other bands. This is known as the Gram-Schmidt process and the general formula for this is seen in equation 10.

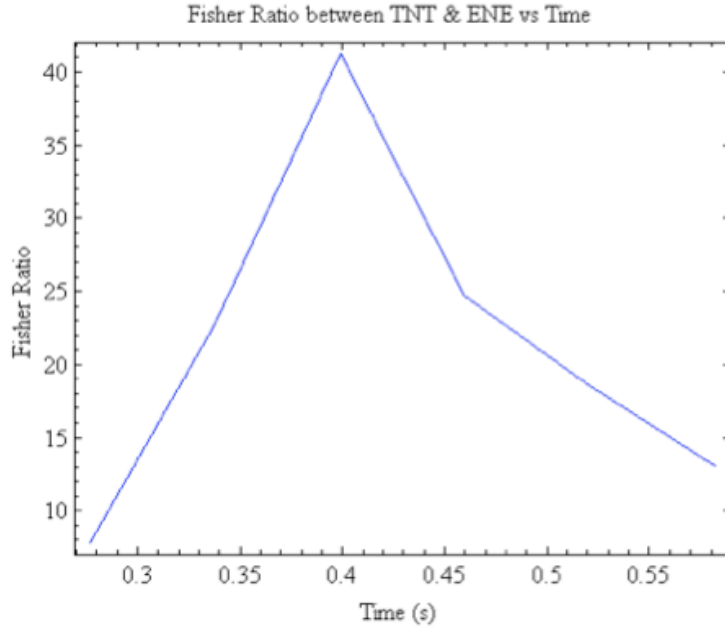


Figure 39. FR versus time using the best bands selected from the three-band search.

$$\text{proj}_{\mathbf{u}} \mathbf{v} = \frac{\langle \mathbf{u}, \mathbf{v} \rangle}{\langle \mathbf{u}, \mathbf{u} \rangle} \mathbf{u} = \langle \mathbf{u}, \mathbf{v} \rangle \frac{\mathbf{u}}{\langle \mathbf{u}, \mathbf{u} \rangle}, \quad (10)$$

Analyzing 3 bands this process yield the specific equation 11, 12, and 13 seen below.

$$\mathbf{u}_1 = \mathbf{v}_1, \quad (11)$$

$$\mathbf{u}_2 = \mathbf{v}_2 - \text{proj}_{\mathbf{u}_1} \mathbf{v}_2, \quad (12)$$

$$\mathbf{u}_3 = \mathbf{v}_3 - \text{proj}_{\mathbf{u}_1} \mathbf{v}_3 - \text{proj}_{\mathbf{u}_2} \mathbf{v}_3 \quad (13)$$

When applied to the data, this process should identify the small aspects from each band that are very difference from each other and provide the large FRs observed. Using the same bands that yielded a FR=41.3, 4970cm⁻¹, 5015cm⁻¹, and 5055cm⁻¹, produces vectors components that have key differences between the TNT and ENE cases. This is seen in Figure 40, which compares the orthonormal components from TNT and ENE events. Band 2 in Figure 40b depicts the TNT and ENE vectors are perpendicular to each other, which supports the large discrimination capability calculated earlier. There are two ENE bands

that are not perpendicular to the TNT events and are both from 100kg ENE2 events. With the exception of these two cases, Figure 40 indicates that there is likely a physical difference between TNT and the ENE variations that can provides a good classification capability in this region. The cause of this difference between the two data classes remains unknown but a small possibility remains that is could be an artifact of the collection method. Because the TNT and ENE events from BFII were collected in a mixed order it is unlikely that this is identifying differences within the atmosphere and the table describing the weather conditions is presented in Table 3 in chapter 2.

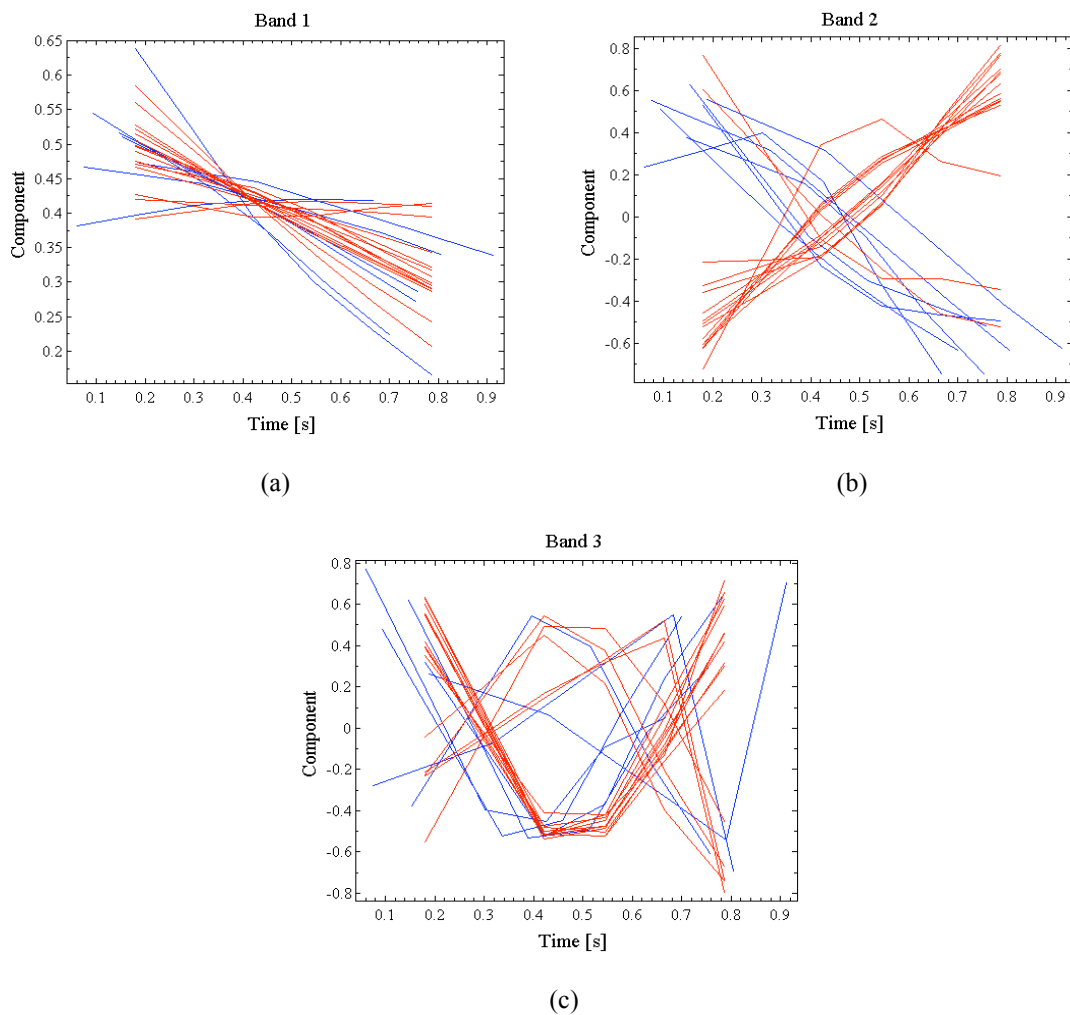


Figure 40. The orthonormal components from the best three bands using the BFII spectral data to derive integrated intensities that produced a FR=41.3 between TNT described by the red lines and ENE represented by a blue lines for (a) band 1 (b) band 2 (c) band 3

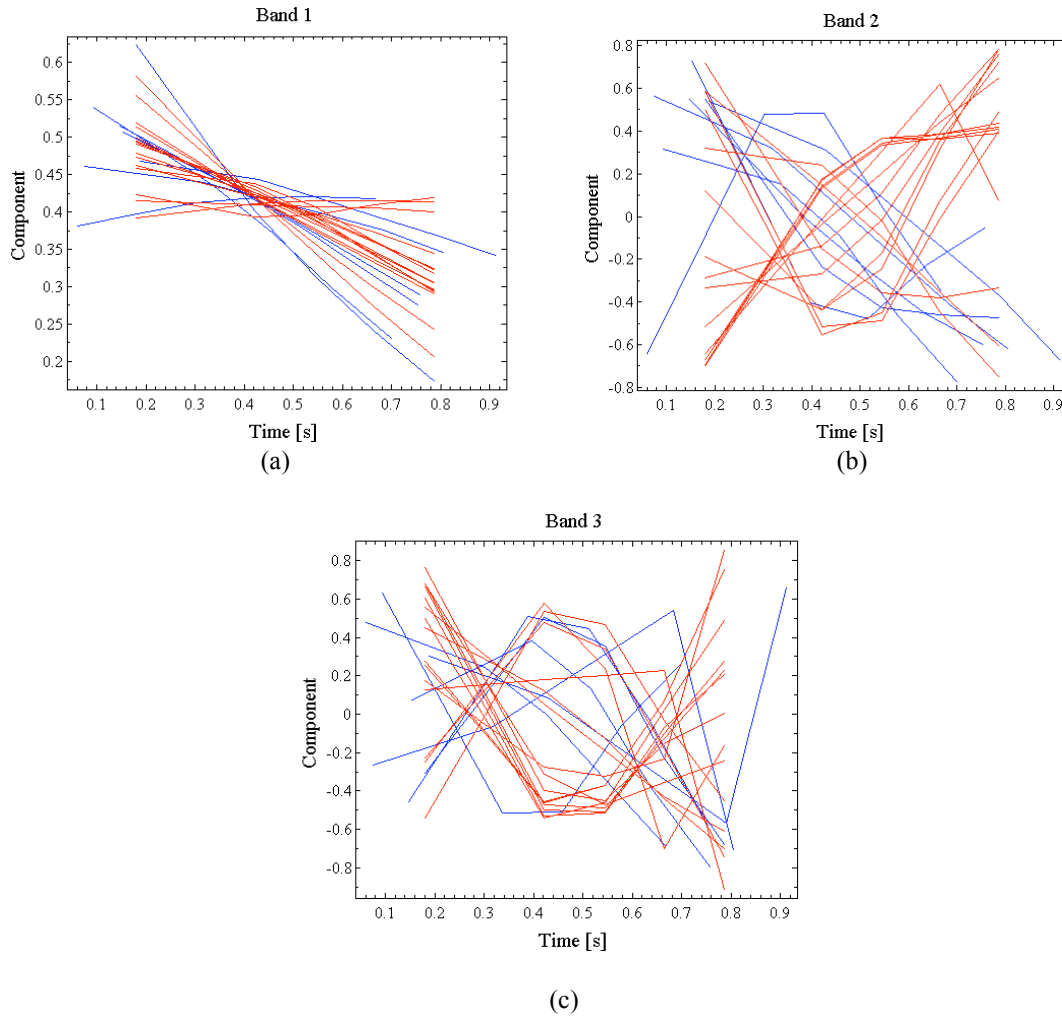


Figure 41. The orthonormal components from the best three bands using the model's spectrum to derive an integrated intensity which produced a FR=5.5 between TNT, described by the red lines, and ENE, represented by a blue lines, for (a) band 1 (b) band 2 (c) band 3

To provide a direct comparison to the simulated data from the model the same methods were applied using the same bands identified that produced the optimal FR for the three-band solution. Using the model's spectrum and integrating over using the respective band provided a FR=5.5 which shows little discrimination capability. This indicates that the model does not account for the feature that is providing the classification capability in the real data. The orthonormal vectors from the model are shown in Figure 41 below. Unlike Figure 40, there is a small difference between the ENE and TNT events. This demonstrates the utility of using a pattern recognition algorithms to identify areas of interest that may of gone unnoticed.

Four Bands.

The four-band search results were very similar to the three-band search and had higher FR results across the entire spectrum. This was likely do to using the same three-bands from the three-band FR spike with added one more. Because of the amount of data present in the four band results were not thoroughly examined since the cause behind the three-band FR remained unknown and the majority of the identified bands were from this region. Also due to the extended time required to process the four-band search was only run using the complete data set.

The multi-band search key finding was from the three-band search with identified the FR spike, which produced a FR double that from the five-band radiometric model. The problems that exists within this is that the three bands used to derive these FRs appear to be highly correlated in nature which do not support the ability to perform clear classification between the events. For the FR spike to be real, the differences between the classes need to be very different from each other to allow for reliable discrimination. This study did not conclusively determine if the FR spike observed actually indentifies a region of high discrimination of is the result of something else present within the data.

V. Conclusion

5.1 Summary of Key Finding

1. A radiometric model to classify TNT and ENE HE fireballs was derived within the MWIR, 1800-6200 cm^{-1} , using five spectral bands.
 - The model used the following bands 2120-2280 cm^{-1} , 2530-2630 cm^{-1} , 3885-4375 cm^{-1} , 4480-4590 cm^{-1} , 4750-5100 cm^{-1} to compute the five fit parameters; temperature, area, the particulate absorption coefficient κ_p , H₂O and CO₂ concentrations.
 - In terms of the magnitude of fit residuals, the radiometric model performs as well as the spectral model. Estimates of temperature, size, and the soot absorption coefficient are comparable with results derived from the spectral model. Water and carbon dioxide concentrations did not compare well with errors of 333%; however, the hydrogen-to-carbon ratio derived from them could still be used to discriminate the two different explosive classes.
 - The five band-integrated intensities are not good features for classification by Fisher linear discrimination with a Fisher ratio of FR=4. However, using the radiometric model to interpret the intensities in terms of five new features—temperature, size, soot absorption, H₂O, and CO₂ concentrations—enables robust classification capability with a FR=23.
2. A revised radiometric model was developed to correct for the poor estimation of the selective gas emitters.
 - Bands for the revised radiometric model were placed at 4350-4530 cm^{-1} , 6000-6200 cm^{-1} , 3850-4350 cm^{-1} , 3200-3600 cm^{-1} and 4700-5800 cm^{-1} to derive the five fit parameters.
 - Concurrently fitting used in the revised radiometric model to calculate the five fit parameters allows for more accurate estimation of the selective gas emitter concentrations.
 - The revised radiometric model provided a better fit with lower RMSE than the original radiometric model did. Agreement between spectral and radiometric estimates of H₂O and CO₂ concentrations were much improved with differences of 17%

3. Using integrated intensities over three distinct bands over the spectral region $4900\text{-}5100\text{cm}^{-1}$, Fisher linear discrimination yields a large separation between the TNT and ENE events with a Fisher ratio of $\text{FR}=41$.
- Various combinations of bands yielded good Fisher ratios, and the following bands yielded the highest ($\text{FR}=41$) value: 4970 , 5015 , and 5055 cm^{-1}
 - The spectrum of ENE and TNT within this region appear very similar, indicating that subtle differences are important to the classification problem.
 - The three integrated intensities are highly correlated with one another. The small part of the signal that is not correlated is important in discriminating the two classes. Gram-Schmidt orthogonal projections of the three intensity profiles exhibit notable differences when comparing TNT and ENE events.
 - The small differences between the TNT and ENE spectra which enabled successful discrimination are not accounted for by the spectral model. Integrated intensities computed from the spectral model over the same three bands previously identified during the FLD three-band search produced a $\text{FR}=5.5$, in contrast with $\text{FR}=41$ when applied to actual data.

5.2 Discussion of the Key Findings

This work has shown that with a careful selection of bands linked to the spectral properties present with those bands, a combination of five radiometric bands can be used in place of a collecting an entire spectrum to model and classify TNT and ENE HE fireballs from each other. The radiometric model produced comparable results to the spectral model with respect to calculating the temperature, size, and the soot absorption constant, but did a poor job in accurately reproducing the H_2O and CO_2 concentrations with a deviation as large as 333%. Even with these discrepancies the radiometric model was able to separate the TNT and ENE as the HCR between them maintained the ratios with respect to the relative stoichiometry. This proves that while the radiometric model isn't perfect, it's maintaining known physical differences between the two classes.

To correct for the errors encountered, a revised radiometric model was implemented. Excluding data below 3200cm^{-1} reduced the spectral region for the radiometric model. This removed the assumption

that emissivity was equal to one in the original band 1, which could have been responsible for some of the error encountered. The method of fitting the data was also adjusted by concurrently fitting four of the fit parameters. This reduced the error present between the spectral models computed fit parameters and the original radiometric fit parameters. It also produced all five fit parameters to within 16% of the spectral model's parameters, which is a vast improvement over the original radiometric model for the two test cases used. This proves that a radiometric model can be used to replace a spectral model and achieve comparable results. The positive results from the two test cases used in the revised radiometric model strongly suggest that the remaining data be analyze. Doing so may highlight additional revisions that could improve the model performance as the original radiometric model did and add statistical confidence to the methods used.

Using the fit parameters provided much better discrimination than using the raw integrated intensities from the five-band radiometric model. This demonstrates that the non-linear interpretation of the intensities into fit parameters provides an enhanced discrimination capability when the FR was used as a measure of classification.

The reduced band search showed a large discrimination potential in regions not previously examined centered at 5000cm^{-1} . An understanding this FR spike observed in the three and four-band searches needs to be exhausted. If it does reveal to be a real features the impact on the working fireball model could be significant. Contrarily if they are found to be artifacts of the data the discrimination capability then a larger emphasis should be placed on intelligent placement and not pattern recognition. The direct comparison between the calculated FRs by using either the integrated intensities or the features they produced is drastic. Using the features resulted in a FR that was five times larger than that of just using the collected intensities. Currently the data suggests that the collections at the beginning of the detonation provide the highest discrimination capability when the time-matched data is used.

It was found that a phenomenological model successfully enabled the re-interpretation of band-integrated intensities as features that could be used to discriminate two different classes of explosives. In almost all cases, the raw band-integrated intensities did not afford the same discrimination capability. However, by systematically searching for the best set of bands, a narrow region was found in which the

discrimination capability *using raw intensities* exceeded what was possible using the phenomenological model to interpret those intensities. This illustrates the synergistic relationship that can exist between the disciplines of modeling and pattern recognition when both are being used to understand and exploit features in data. For example, phenomenological modeling can enhance classification as non-linear, physics-based relationships can be used to efficiently reduce dimensionality and provide “orthogonal” features for classification. On the other hand, statistical classification methodologies may uncover important features for discrimination that are not explained by the phenomenological model, thus indicating ways in which it can be improved.

With a proof of concept with the five-band radiometric model achieved a real test using a combination of radiometers should be performed. The findings may provide an answer to some of the fit parameters discrepancies observed between the spectral and radiometric model. Concerning the multi-band search the observed FR spikes need to be further investigated to determine the validity and utility of the result. If a feature does exist that region it needs to be identified and mapped back the physical properties responsible for it. Additionally the intensity and spectral signature needs to be examined within these regions containing the FR spikes.

5.3 Future Research

Future research on this topic would be a direct expansion of this work with a further examination of the features should be completed with a focus on reduction of required bands or features. This would investigate if assumptions could be made to achieve similar discrimination results with fewer collection sources. Additionally the temporal aspects of HE fireballs need to be thoroughly examined, as a detailed understanding of this aspect remains relatively unexplored in terms of its relationship with the EO signature and classification purposes. This would add another dimension to the model and could allow for previously unused temporal information already collected by a radiometer. Finally the data sets and collections of HEs should be increased to increase the statistical confidence on previous, current and future research. The limitations of the number of data sets have been a consistent factor in determining the statistical robustness of the analysis.

The potential for the uses of five-banded radiometric model is wide in variety. By allowing for smaller and more robust sensors to be able to provide passive detection capabilities and reliable characterization of known signatures could lead to several new sensor designs. These systems could be fielded on a variety of land, sea, air, and space platforms. Also if these conceptual sensors are positioned to collect a HE fireball it could provide timely information concerning the chemical make up of the detonation.

Appendix

Interferogram time corrections

The data for this work was examined to ensure that the event timelines were properly aligned with each other. A common problem with collecting fast changing events is directly related to the movements of the mirror inside of the spectrometer and that it does not move at a uniform velocity. As the mirror slides back and forth it slightly speeds and up and down as it changes directions, which is an expected property of the mechanical device. During collection the data is time tagged once during the mirrors path. The problem with short-lived events is that it's very difficult to match the time tagging with the exact moment the first emissions from the source hit the detector. This leads to a small time tagging issue with the point of first detection. The data was originally time tagged at the very beginning of the scan at t_o with the approximate time to complete a scan t_s being 0.121s. To perform a correction, the speed of the mirror was assumed to move at a constant linear velocity to reduce computational complexity. While this is not exact characterization due to the non-linear speed of the mirror, it does provide an overall improvement from the original time recorded. The center burst of the interferogram contains all of the information concerning the total integrated observed intensity. Since the tagged time does not match this, an additional correction is made to reference the center burst with respect to the offset detection time to replace the beginning of the scan time. The center burst occurs half way through the scan ($t_s/2$) and is added to scan 2 as seen in Figure 42, to reference where the derived intensity was estimated at. Since the event did not start at $t_s/2$, but at some offset time, t_{off} , this difference must also be accounted for. The relationship between the known optical path distance (OPD) and the total scan time is used to calculate t_{off} , as seen in equation 14, where N_i is the initial position of the mirror at first detection and N_{tot} is the total distance traveled by the mirror.

$$t_{off} = t_s \left(1 - \frac{N_i}{N_{tot}} \right) \quad (14)$$

Once t_{off} is known, all of the relevant information to perform the correction is now known. Since the derived intensity from scan 1 is incorrect because the event occurred after the center burst providing an inaccurate estimate of intensity for that scan, the correction must be made with respect to scan 2 as seen in Figure 42. Equation 15 shows the total correction that is required to properly reference the center burst in scan 2.

Interferogram Time Correction

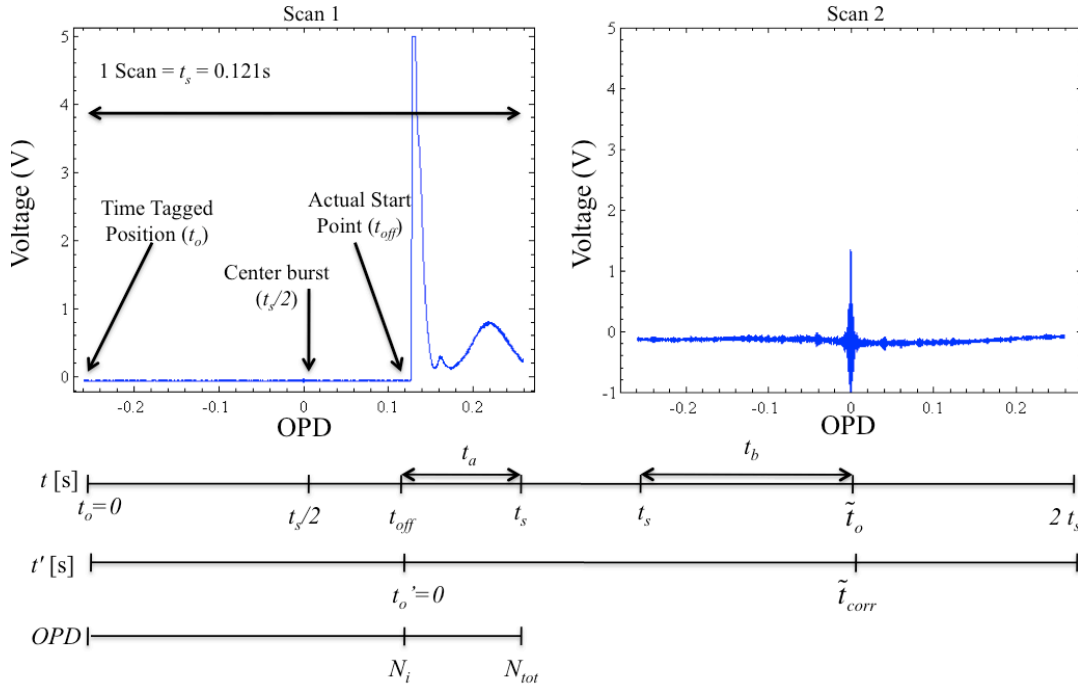


Figure 42. Interferogram from the MR-154 during the BFII collection observing a detonation out of since with the intensity calculation.

$$\tilde{t}_o = t_a + t_b = t_s \left(1 - \frac{N_i}{N_{tot}} \right) + \frac{t_s}{2} = t_s \left[\frac{3}{2} - \frac{N_i}{N_{tot}} \right] \quad (15)$$

This is further simplified by substituting in the values for t_a and t_b shown in equation 16.

$$t_a = t_s - t_{off} = t_s \left(1 - \frac{N_i}{N_{tot}} \right) \longrightarrow t_a = t_s - t_{off} \longrightarrow t_b = \frac{t_s}{2} \quad (16)$$

Combining equations 15 & 16 into 14 yields equation 17 shifts the center burst time to correctly reference the intensity derived from the center burst with respect to the time of first detection.

$$\tilde{t}_{corr} = \frac{3t_s}{2} - t_a = \frac{t_s}{2} + t_{off} \quad (17)$$

Table 9. table showing the corrected times of the data and the start, end and delta in seconds of each observed event and whether or not it was used in the analysis.

Blast number	Type	Size (kg)	Start Time (s)	End Time (s)	Delta (s)	Used
1	TNT	10	0.23	0.47	0.24	N
2	ENE0A	10	NA	NA	NA	N
3	ENE1	10	0.06	0.3	0.24	N
4	ENE2	10	0.16	0.28	0.12	N
5	ENE1	50	0.15	0.63	0.48	Y
6	ENE1	50	0.18	0.66	0.48	Y
7	TNT	10	0.11	0.23	0.12	N

8	TNT	50	NA	NA	NA	N
9	ENE1	50	NA	NA	NA	N
10	TNT1	50	0.1	0.58	0.49	Y
11	TNT2	50	0.28	0.64	0.36	Y
12	ENE2	50	0.18	0.54	0.36	Y
13	ENE0	50	0.07	0.32	0.24	N
14	ENE0	50	0.09	0.21	0.12	N
15	TNT	10	0.12	0.24	0.12	N
16	TNT	100	NA	NA	NA	N
17	ENE0	50	0.07	0.19	0.12	N
18	ENE0	50	0.18	0.3	0.12	N
19	ENE2	50	0.06	0.55	0.49	Y
20	ENE2	50	NA	NA	NA	N
21	TNT	10	0.14	0.26	0.12	N
22	ENE1	100	0.18	1.28	1.09	Y
23	ENE1	100	0.23	1.2	0.97	Y
24	TNT	50	NA	NA	NA	N
25	TNT	50	0.08	0.93	0.85	Y
26	ENE0	100	0.09	0.82	0.73	Y
27	ENE0	100	0.1	0.95	0.85	Y
28	ENE2	100	0.09	1.66	1.58	Y
29	ENE2	100	0.18	1.51	1.33	Y
30	ENE1	100	0.18	1.51	1.33	Y
31	TNT	50	0.15	0.87	0.73	Y
32	TNT	1000	0.06	2.96	2.9	Y
33	ENE2	1000	0.11	2.05	1.94	Y
34	TNT	100	0.15	1.48	1.33	Y
35	ENE1	1000	0.17	2.1	1.93	Y
36	TNT	100	0.19	1.76	1.57	Y
37	ENE2	1000	0.17	1.98	1.81	Y
38	ENE2	100	0.15	1.11	0.97	Y
39	ENE2	50	0.06	0.79	0.73	Y
40	TNT	50	0.09	0.94	0.85	Y
41	ENE2A	50	0.08	0.93	0.85	Y
42	ENE2A	50	0.1	0.94	0.85	Y
43	ENE2A	50	0.18	0.91	0.73	Y
44	TNT	50	0.18	0.91	0.73	Y

Bibliography

1. Gross, Kevin C. "Phenomenological model for infrared emissions from high-explosive detonation fireballs" Ph. D. dissertation, AFIT/DS/ENP/07-3, Air Force Institute of Technology, 2005.
2. Fan, W. H.; Burnett, A.; Upadhyya, P.C.; Cunningham, J.; Linfield, E. H.; Davies, A. G. "Far-infrared spectroscopic characterization of explosives for security applications using broadband terahertz time-domain spectroscopy" *Applied Spectroscopy*, v61, n 6, p 638-643, June, 2007.
3. Dills, Anthony N. "Classification of battle space detonations from temporally-resolved multi-band imagery and mid-infrared spectra" Ph. D. dissertation, AFIT/DS/ENP/04-2, Air Force Institute of Technology, 2005.
4. Bell, John R. *Introductory Fourier Transform Spectroscopy*. Academic Press, New York, 1972.
5. Griffiths, P., & De Haseth, J. Theoretical background. Fourier transform infrared spectrometry (2nd ed., pp. 19-30). Hoboken, N.J.: John Wiley & Sons, Inc, 2007.
6. Smith, B. (1996). How an FTIR works. Fundamentals of fourier transform infrared spectroscopy (First ed., pp. 15-22). Boca Raton: CRC Press, 1996.
7. Michelson, A., & Morley, E. (1887). "On the relative motion of the earth and the luminiferous ether". *The American Journal of Science*, 134(203), 333-345.
8. Kick, Hermann, Volker Tank, and Erwin Lindermeir. "Impact of scene changes during data acquisition in Fourier spectroscopy". *Journal of Quantitative Spectroscopy & Radiative Transfer*, 92:447-455, 2004.
9. Dills, Anthony H. and G. P. Perram "Brilliant Flash II Preliminary Test Report from AFIT Sensors." Technical Report, Air Force Institute of Technology, Wright-Patterson AFB, OH, 2003 (unpublished)
10. Duda, Richard O., Peter E. Hart, David G. Stork. *Pattern Classification*, 2nd Ed., John Wiley & Sons, Inc., New York, 2001.
11. Fisher, Bob. "Fisher linear discriminant and dataset transformation." n. pag. http://homepages.inf.ed.ac.uk/rbf/CVonline/LOCAL_COPIES/FISHER/FLD/flld.htm l. 1 July 2004.
12. Gross Kevin C. and G. P. Perram "Using fireball phenomenology to assess the applicability of current and future military sensors to the counter-IED fight."

Presentation, Air Force Institute of Technology, Wright-Patterson AFB, OH, 2008
(unpublished)

13. Clough, S. A., et al. "Atmospheric radiative transfer modeling: A summary of the AER codes." *Journal of Quantitative Spectroscopy & Radiative Transfer*, 233-244, 2005.
14. Dereniak, E. L., and G. D. Boreman. *Infrared Detectros and Systems*. John Wiley & Sons, Inc., 1996.

REPORT DOCUMENTATION PAGE			Form Approved OMB No. 074-0188		
<p>The public reporting burden for this collection of information is estimated to average 1 hour per response, including the time for reviewing instructions, searching existing data sources, gathering and maintaining the data needed, and completing and reviewing the collection of information. Send comments regarding this burden estimate or any other aspect of the collection of information, including suggestions for reducing this burden to Department of Defense, Washington Headquarters Services, Directorate for Information Operations and Reports (0704-0188), 1215 Jefferson Davis Highway, Suite 1204, Arlington, VA 22202-4302. Respondents should be aware that notwithstanding any other provision of law, no person shall be subject to a penalty for failing to comply with a collection of information if it does not display a currently valid OMB control number.</p> <p>PLEASE DO NOT RETURN YOUR FORM TO THE ABOVE ADDRESS.</p>					
1. REPORT DATE (DD-MM-YYYY) 26-03-2009		2. REPORT TYPE Master's Thesis		3. DATES COVERED (From - To) Mar 2008 - Mar 2009	
4. TITLE AND SUBTITLE Advanced Radiometry for High Discrimination Explosive Fireball Discrimination			5a. CONTRACT NUMBER		
			5b. GRANT NUMBER		
			5c. PROGRAM ELEMENT NUMBER		
6. AUTHOR(S) Slagle, Steven, E., Captain, USAF			5d. PROJECT NUMBER		
			5e. TASK NUMBER		
			5f. WORK UNIT NUMBER		
7. PERFORMING ORGANIZATION NAMES(S) AND ADDRESS(S) Air Force Institute of Technology Graduate School of Engineering and Management (AFIT/EN) 2950 Hobson Way WPAFB OH 45433-7765			8. PERFORMING ORGANIZATION REPORT NUMBER AFIT/GEO/ENP/09-M02		
9. SPONSORING/MONITORING AGENCY NAME(S) AND ADDRESS(ES) This space intentionally left blank			10. SPONSOR/MONITOR'S ACRONYM(S)		
			11. SPONSOR/MONITOR'S REPORT NUMBER(S)		
12. DISTRIBUTION/AVAILABILITY STATEMENT APPROVED FOR PUBLIC RELEASE; DISTRIBUTION UNLIMITED.					
13. SUPPLEMENTARY NOTES					
14. ABSTRACT The high explosive fireball phenomenological model for the mid wave infrared spectrum, developed by AFIT, performs classification from spectral signatures was modified to use radiometric intensities. Five bands were sequentially fit to derive the five physical fit parameters describing the fireball's temperature, size, soot absorption coefficient within 16% and emissions from the H2O and CO2 concentrations within 333% of the spectral model. This was improved by changing the model's the band sizes, center, and fitting methods where all five fit parameters were matched to within 17% of spectral model. This demonstrated that a combination of radiometric intensities could be used in place of the spectral data. Interpreting the intensities into fit parameters provided and increased in classification capability with a Fisher Ratio (FR) =23 as opposed to a FR=4 when using the five raw intensities. A systematic search was performed to investigate classification potential using two, three and four radiometric bands combinations. The two-band search yielded a maximum FR of 6, a poor classification capability where the three and four-band search highlighted a highly confined spectral region centered at 5000cm-1 with a FR=41.					
15. SUBJECT TERMS High Explosive, Fireball, Detonation, Improvised Explosive Device (IED), Fourier-Transform Spectroscopy, Radiative Transfer, Radiometric Intensity, Classification, Fisher Ratio, Fisher Linear Discrimination,					
16. SECURITY CLASSIFICATION OF:		17. LIMITATION OF ABSTRACT	18. NUMBER OF PAGES	19a. NAME OF RESPONSIBLE PERSON	
REPORT	ABSTRACT			c. THIS PAGE	19b. TELEPHONE NUMBER (Include area code)
U	U	U	81	Dr Kevin C. Gross (AFIT/ENP) (937) 255-3636, ext 4558; e-mail: kevin.gross@afit.edu	

Standard Form 298 (Rev. 8-98)

Prescribed by ANSI Std. Z39-18